

# A turbulence dissipation inhomogeneity scaling in the wake of two side-by-side square prisms

J.G. Chen<sup>1</sup>, C. Cuvier<sup>1</sup>, J.-M. Foucaut<sup>1</sup>, Y. Ostovan<sup>1</sup> and J.C. Vassilicos<sup>1†</sup>

<sup>1</sup>Univ. Lille, CNRS, ONERA, Arts et Metiers Institute of Technology, Centrale Lille, UMR 9014 - LMFL - Laboratoire de Mécanique des Fluides de Lille - Kampe de Fériet, F-59000 Lille, France

(Received xx; revised xx; accepted xx)

We experimentally study how the turbulent energy dissipation rate scales in the cross-stream direction of turbulent wake flows generated by two side-by-side square prisms. We consider three different such turbulent flows with gap ratios  $G/H = 1.25, 2.4$  and  $3.5$ , where  $G$  is the distance between the prisms and  $H$  is the prism width. These three flows have very different dynamics, inhomogeneities and large-scale features. The measurements were taken with a multi-camera particle image velocimetry (PIV) system at several streamwise locations between  $2.5H$  and  $20H$  downstream of the prisms. After removing the large-scale most energetic coherent structures, the normalised turbulence dissipation coefficient  $C'_\epsilon$  of the remaining incoherent turbulence is found to scale as  $C'_\epsilon \sim (\sqrt{Re_L}/Re'_\lambda)^{3/2}$  along the highly inhomogeneous cross-stream direction for all streamwise locations tested in all three flows and for all three inlet Reynolds numbers considered.  $Re'_\lambda$  and  $Re_L$  are, respectively, a Taylor length-based and an integral length-based Reynolds number of the remaining incoherent turbulence.

## 1. Introduction

In the framework of Kolmogorov's (K41) equilibrium cascade theory for homogeneous turbulence (Kolmogorov 1941*a,b,c*; Batchelor 1953), the energy dissipation rate  $\bar{\epsilon}$  in the turbulent flow can be scaled as

$$\bar{\epsilon} = C_\epsilon \mathcal{U}^3 / L \quad (1.1)$$

where  $\mathcal{U}$  is the characteristic velocity scale of the energy-containing eddies, and their size is captured by the integral length scale  $L$ .  $C_\epsilon$  is a non-dimensional constant (independent of time, position and Reynolds number) of order unity at sufficiently large Reynolds number. Equation (1.1) is sometimes referred to as the Taylor-Kolmogorov relation because it first appeared (without much justification) in Taylor (1935). As mentioned by Rubinstein & Clark (2017), “if the idea of ‘equilibrium’ in turbulence and the Taylor-Kolmogorov relation were restricted to static spectra alone, they would have only limited importance. We arrive at something more general by recalling that the importance of the K41 equilibrium is the hypothesis that it occurs in any turbulent flow.” This made equation (1.1) “one of the cornerstone assumptions of turbulence theory”, quoting Tennekes & Lumley (1972). It provides a concise and straightforward way to estimate the energy dissipation rate in the flow and to model eddy viscosities in Reynolds-averaged Navier-Stokes models of turbulence (see Pope 2000). It also indicates an essential feature of the equilibrium energy cascade: the energy dissipation level in the flow is dictated by the large-scale eddies, irrespective of fluid kinematic viscosity  $\nu$ , instantaneously.

In the past decade, it has been observed in protracted initial decay regions of various

† Email address for correspondence: john-christos.vassilicos@centralelille.fr

turbulent flows where energy spectra have clear power law ranges with exponents close to Kolmogorov's  $-5/3$ , that the turbulence dissipation rate does not obey (1.1) with constant  $C_\epsilon$  but that  $C_\epsilon$  depends on local and global Reynolds numbers (see the review of Vassilicos 2015) as follows:

$$C_\epsilon \sim Re_G^{m/2}/Re_\lambda^n (\neq Const) \quad (1.2)$$

where  $m \approx 1$  and  $n \approx 1$ ;  $Re_G \equiv U_\infty L_g/\nu$  is the global Reynolds number based on the incoming velocity  $U_\infty$  and a characteristic size of the turbulence generator  $L_g$ ,  $\nu$  being the kinematic viscosity; and  $Re_\lambda \equiv u_k \lambda/\nu$  is the local (in streamwise direction) Reynolds number based on a local velocity scale  $u_k$  representing the local turbulent kinetic energy and the local Taylor length-scale  $\lambda$ . The observation of relation (1.2), which is referred to as the non-equilibrium turbulence dissipation scaling (Vassilicos 2015), was first reported by Seoud & Vassilicos (2007) in an approximately locally homogenous and isotropic turbulent flow generated by a fractal grid. Later on, it was also confirmed in various types of fractal grids and observed in a variety of other turbulent flows, including fractal/multiscale and regular grid turbulence (Valente & Vassilicos 2012; Isaza *et al.* 2014; Hearst & Lavoie 2014; Nagata *et al.* 2013, 2017), axisymmetric and planar bluff body wakes (Obligado *et al.* 2016; Alves Portela *et al.* 2018; Chongsiripinyo & Sarkar 2020), planar jets (Cafiero & Vassilicos 2019), turbulent boundary layers (Nedić *et al.* 2017), and both forced and decaying periodic turbulence (Goto & Vassilicos 2015) in which case  $Re_\lambda$  is local in time. Most recently, Ortiz-Tarin *et al.* (2021) found a non-equilibrium dissipation scaling with an exponent  $n = m$  different from 1 in the high Reynolds number wake of a slender (rather than bluff) body.

The turbulence dissipation scaling has a profound influence on basic turbulent flow properties such as mean flow profile streamwise evolution and the turbulent/non-turbulent interface propagation velocity in self-preserving boundary-free turbulent shear flows. The rate of growth of self-similar turbulent jets and wakes is very different in the presence of the non-equilibrium dissipation scaling (1.2) than in the presence of the Taylor-Kolmogorov scaling  $C_\epsilon = Const$  (Nedić *et al.* 2013; Dairay *et al.* 2015; Cafiero & Vassilicos 2019). Similarly, the turbulent/non-turbulent interface propagation velocity is very different in these flows in the presence of one or the other dissipation scaling too (Zhou & Vassilicos 2017; Cafiero & Vassilicos 2020). These differences have been observed in Direct Numerical Simulations (DNS) and laboratory experiments (Nedić *et al.* 2013; Dairay *et al.* 2015; Zhou & Vassilicos 2017; Cafiero & Vassilicos 2019, 2020).

As demonstrated by Goto & Vassilicos (2015, 2016a,b) the turbulence cascade responsible for the dissipation scaling (1.2) is an out of equilibrium non-Kolmogorov cascade with a significant time-lag between the rate of energy loss by the energy-containing eddies and the turbulence dissipation by the smallest ones which, therefore, do not balance instantaneously. The presence of this non-equilibrium cascade is felt in non-stationary conditions, either in time, as in time-evolving periodic turbulence, or in the streamwise directions for flows such as jets, wakes and grid-turbulence. In such flows, the streamwise direction represents time in the frame moving with the streamwise mean flow velocity (e.g. Taylor 1938).

Unlike the Kolmogorov equilibrium cascade and the resulting Taylor-Kolmogorov dissipation scaling which are well established as time-average properties of statistically stationary turbulence that is either homogeneous (even if only locally) or periodic (Kolmogorov 1941b,a,c; Frisch 1995; Vassilicos 2015; Goto & Vassilicos 2015, 2016a; Yasuda & Vassilicos 2018), the dissipation scaling (1.2) is also present in non-homogeneous turbulence, for example turbulent jets and wakes. Turbulence inhomogeneity typically implies production and spatial fluxes of turbulent kinetic energy which must be dissipated by a turbulence cascade mechanism. Given that the non-equilibrium cascade gives rise to a universal relation between the time/streamwise variations of  $C_\epsilon$  and  $Re_\lambda$  (relation (1.2)) in a universality

class of flows currently known to include self-similar jets and wakes, decaying grid and periodic turbulence, and forced periodic turbulence, could it also give rise to a universal relation between space variations of  $C_\epsilon$  and  $Re_\lambda$ ? If such a relation exists and is the same for different inhomogeneity structures, then one should seriously consider the possibility that it is a reflection of a turbulence cascade which somehow universally relates turbulent kinetic energy, turbulence dissipation and size of energy containing eddies, the three turbulence quantities involved in  $C_\epsilon$  and  $Re_\lambda$ . Indeed, the turbulence cascade is one mechanism involved in the turbulent kinetic energy balance which may be essentially the same for a range of types of inhomogeneity. Of course, if such a relation exists for some universality class of turbulence inhomogeneities and if it does indeed reflect a turbulence cascade mechanism, then this turbulence cascade will have to be a non-Kolmogorov cascade simply because it will fundamentally concern non-homogeneous turbulence.

The first question we therefore ask in this paper is whether a relation of general validity exists between  $C_\epsilon$  and  $Re_\lambda$  in the transverse direction of a class of inhomogeneous turbulent flows. The second question we ask in this paper is whether such a non-homogeneous dissipation scaling, if it exists, has anything in common with the non-equilibrium/non-stationarity dissipation scaling (1.2). The non-equilibrium cascade which gives rise to (1.2) is such that  $C_\epsilon$  grows or decays when  $Re_\lambda$  decays or grows in the streamwise direction: for example,  $C_\epsilon$  grows as  $Re_\lambda$  decays in axisymmetric turbulent wakes, decaying grid turbulence and decaying periodic turbulence (Dairay *et al.* 2015; Vassilicos 2015; Goto & Vassilicos 2015, 2016a,b); and  $C_\epsilon$  decays as  $Re_\lambda$  grows in planar turbulent jets (Cafiero & Vassilicos 2019). Does something similar happen in transverse/cross-stream directions? Whether it is worth investigating a new concept of inhomogeneous turbulence cascades and its potential relations with non-equilibrium cascades will be determined by the results of the present study and is a question which must be left for future research.

To address the two questions raised above, we examine cross-stream profiles of turbulent kinetic energy, integral length-scale and turbulence dissipation in the wakes of side-by-side pairs of square prisms. It has been established in previous investigations that there are mainly three flow regimes in such flows (e.g. Sumner *et al.* 1999; Alam *et al.* 2011; Yen & Liu 2011): (a) when  $G/H \leq 1.2 \sim 1.3$  where  $G$  is the center-to-center distance between the prisms and  $H$  is the side-length/width of the square prism (see figure 1), the flow is similar to that of a single bluff body, so this case is referred to as ‘single-bluff-body regime’; (b) for  $G/H$  between  $1.2 \sim 1.3$  and  $2.2 \sim 2.5$ , the flow switches intermittently from one prism to the other, resulting in one wide and one narrow vortex streets in the wake. This flow case is the ‘bistable regime’ or ‘asymmetric wake regime’ (e.g. Kim & Durbin 1988); (c) when  $G/H > 2.2 \sim 2.5$ , the flow loses the bistability of the previous regime and two coupled vortex streets form in the wake, either in in-phase or in anti-phase mode (e.g. Alam & Zhou 2013). This case is referred to as ‘couple-street regime’. Note that the critical  $G/H$  values which demarcate different flow regimes are affected by the inlet Reynolds number (Xu *et al.* 2003).

In the present study, we follow Avelar (2019) and chose three gap ratios,  $G/H = 1.25, 2.4$  and  $3.5$ , one  $G/H$  value for each one of the three different flow regimes just mentioned. This provides significant variability in flow types and turbulence inhomogeneity for a systematic investigation of the relation between  $C_\epsilon$  and  $Re_\lambda$  in qualitatively different flows obtained by simple adjustments of inlet conditions without changing global Reynolds number. To also assess the effect of global Reynolds number, each  $G/H$  case is studied under at least two incoming velocities (see section 2).

The paper is organised as follows. Section 2 describes the experiments. In section 3, we compare the different flow fields obtained for different gap ratios to evidence the different large-scale features of the turbulence and the different turbulent flow inhomogeneities in the

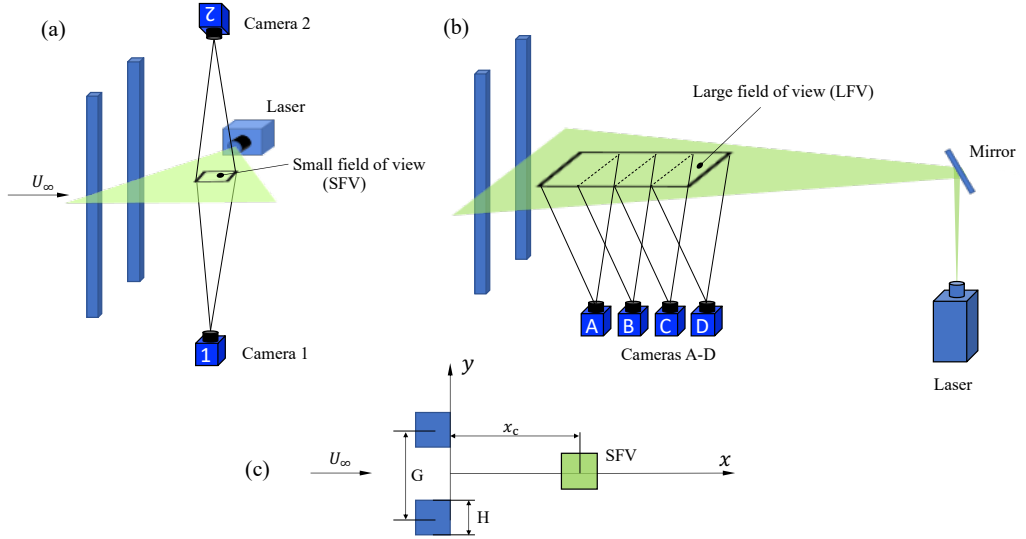


Figure 1: (a) PIV set up for the energy dissipation rate measurements. (b) PIV set up for the integral length scale measurements. (c) The coordinate system normal to the prisms's spanwise direction and definitions of  $G$ ,  $H$  and  $x_c$ . All fields of view in (a), (b) and (c) and laser sheets in (a) and (b) are in the horizontal ( $x, y$ ) plane.

three flows. The scaling of the energy dissipation rate is studied in section 4, including the result both with and without the energy of the coherent motions. Conclusions are given in section 5 and the Appendix gives some information on the proper orthogonal decomposition method used in the study.

## 2. Experimental details

The experiment was carried out in the boundary layer wind tunnel of the Lille Fluid Mechanics Laboratory (LMFL). The test section of the wind tunnel is 2m wide by 1m high and 20m long. The wind tunnel operates in a closed loop and the test section is transparent on all four sides to allow extensive use of optical techniques. The temperature is regulated to  $\pm 0.15\text{K}$  using a heat exchanger located in the plenum chamber. The external speed is controlled by adjusting the fan speed with a stability of better than 0.5%. Both parameters are fully computer controlled. More details about the wind tunnel are available in Carlier & Stanislas (2005). For the present study, two aluminium square prisms with same  $H = 0.03\text{m}$  were used and vertically positioned in the test section at about 5m downstream of the test section's entrance (figure 1a). Experimental measurements were taken with three different center-to-center gap distances  $G$  between the two prisms (figure 1c), i.e.  $G = 1.25H$ ,  $2.4H$  and  $3.5H$ , and three incoming velocities  $U_\infty = 5, 6, \text{ and } 7.35\text{m/s}$  (measured with a pitot tube 0.45m upstream of the prisms) corresponding to global Reynolds numbers  $Re = U_\infty H / \nu = 1.0, 1.2 \text{ and } 1.5 \times 10^4$  respectively. The pitot tube was removed after measuring the incoming velocity. Experiments with different  $G/H$  cases were run for each  $Re$  as listed in table 1.

To obtain  $C_\epsilon$  and  $Re_\lambda$  we need to measure estimates of turbulent dissipation rate, turbulent kinetic energy and integral length scale and we had to use different PIV set ups for the measurements of turbulent dissipation on the one hand (figure 1a) and integral length scale on the other (figure 1b). The energy dissipation rate  $\bar{\epsilon}$  was measured with a system of two cameras (figure 1a). The system comprises an Innolas 2x150mJ YAG laser at 10Hz with

$Re$	$1.0 \times 10^4$			$1.2 \times 10^4$			$1.5 \times 10^4$
$G/H$	1.25	2.4	3.5	1.25	2.4	3.5	3.5
Cases	SFV7	SFV2.5	SFV7	SFV14	SFV14	SFV14	SFV20
	SFV14	SFV5	SFV14	SFV20	SFV20	SFV20	
	SFV20	SFV10	SFV20				
		SFV20					
Area ( $\Delta x \times \Delta y$ )	$1H \times 0.9H$			$1H \times 0.9H$			$1H \times 0.9H$

Table 1: Details of the small fields of view (SFV).

$Re$	$1.0 \times 10^4$			$1.2 \times 10^4$			$1.5 \times 10^4$
$G/H$	1.25	2.4	3.5	1.25	2.4	3.5	3.5
$x$ range( $H$ )	0.53 – 24.3			11.1 – 24.9			11.1 – 24.9
$y$ range( $H$ )	-2.4 – 2.9			-2.8 – 3.0			-2.8 – 3.0

Table 2: Details of the large fields of view (LFV).

which a laser sheet is obtained in the horizontal ( $x, y$ ) plane normal to the vertical span of the prisms. This sheet enters from the side of the test section and is 0.3 mm thick. Two sCMOS cameras are positioned on either side of the sheet, one over the top and one under the bottom of the test section, and observe the same region of the flow so as to have two independent measurements of the velocity fields. The calibration was conducted on a transparent grid with cross patterns which allows the same points to be located to within 0.1 pixel on both cameras and therefore generates a common mesh to allow denoising. The idea, following Foucaut *et al.* (2020), is that two independent measurements of the same quantity can be used to estimate and/or remove the noise in statistical calculations (cf. Foucaut *et al.* 2016). We explain how we apply this denoising procedure to the calculation of  $\bar{\epsilon}$  in the following paragraphs. The cameras are equipped with 200 mm Micro-Nikor lenses, the f-stop is adjusted to 8 to obtain particle images of the order of 2 pixels. The magnification is 0.5, and the field of view, which is referred to as small field of view (SFV), is about  $1H$  in streamwise direction by  $0.9H$  in lateral direction (figure 1 a and c). For each gap ratio  $G/H$ , the measurement was taken at several downstream positions along the geometric centreline which crosses mid-distance between the two prisms ( $y = 0$ ), as sketched in figure 1c where  $x_c$  is the streamwise position of the centre of the SFVs. The measurement cases for each  $G/H$  are summarized in table 1. Note that in the table, the cases are referred to as SFV $\mathcal{N}$  where  $\mathcal{N}$  gives an idea in terms of multiples of  $H$  of the approximate streamwise distance  $x_c$  of the centre of the corresponding SFV from the mid-point between the prisms.

The energy dissipation rate  $\bar{\epsilon}$  is estimated based on the assumption of local axisymmetry along the streamwise direction (see George & Hussein 1991) as follows:

$$\bar{\epsilon} = \nu \left[ -\overline{\left(\frac{\partial u}{\partial x}\right)^2} + 2\overline{\left(\frac{\partial u}{\partial y}\right)^2} + 2\overline{\left(\frac{\partial v}{\partial x}\right)^2} + 8\overline{\left(\frac{\partial v}{\partial y}\right)^2} \right] \quad (2.1)$$

where the overbar is an average over time,  $u$  and  $v$  are the fluctuating velocity components in the streamwise and cross-stream directions respectively, and where  $x$  and  $y$  are the streamwise

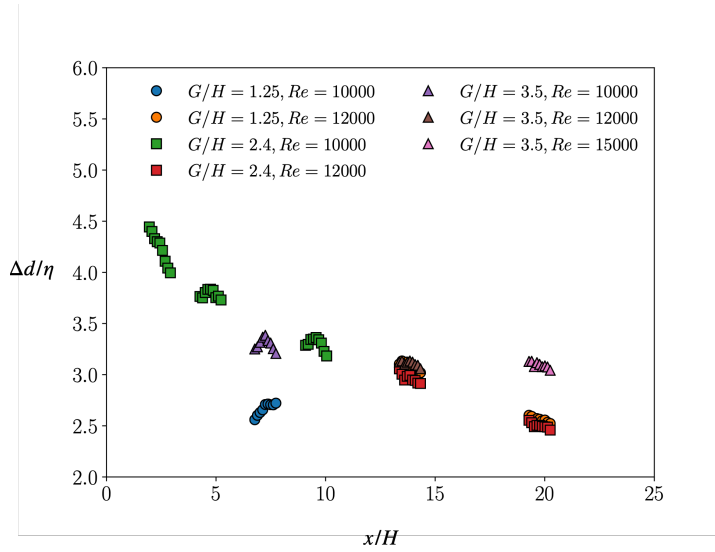


Figure 2: Ratios of the interrogation window size in the SFVs to the local Kolmogorov length scale  $\eta$  at different streamwise positions along the geometric centreline.

and cross-stream spatial coordinates shown in figure 1. Lefeuvre *et al.* (2014) demonstrated that the energy dissipation rate estimated based on the streamwise local axisymmetry assumption is a good representation of the full energy dissipation rate across the stream in the wake of a square prism, and in fact more accurate than the energy dissipation rate estimated based on the locally isotropy assumption, especially in the near wake region.

The velocity fluctuation derivatives in equation (2.1) are obtained from the SFV measurements with a central differencing scheme. The denoising is that of Foucaut *et al.* (2020) and takes advantage of the fact that every term in equation (2.1) is the product of a derivative with itself. One of the two derivatives in this product is obtained from one camera and the other derivative from the other camera. As the noise in the measurements made with one camera is uncorrelated with the noise in the measurements made with the other camera, the average over time (i.e. over different PIV images) of the product of these two derivatives has a very significantly reduced noise contribution. For example, the term  $\overline{(\partial u/\partial x)^2}$  is obtained by time-averaging the product of  $(\partial u/\partial x)$  from one of the two cameras with  $(\partial u/\partial x)$  from the other camera. The same process has been applied to the other mean-square velocity derivative terms in equation (2.1), so that the noise in  $\epsilon$  is significantly reduced.

A different PIV set up is used for the integral length scale measurements (figure 1b), in which case the field of view is referred to as a large field of view (LFV). For these measurements, a 2x220mJ YAG BMI laser at 12Hz was used; the beam quality of this laser makes it possible to produce a sheet with a substantially constant thickness of around 0.8mm over a length of 1m. A system of four sCMOS cameras was positioned to obtain a field of view of 24H (streamwise) by approximately 5.5H (cross-stream) for the smallest Reynolds number  $Re = 1.0 \times 10^4$ , and two sCMOS were used to get a field of view of 14H (streamwise) by 6H (cross-stream) for the two larger Reynolds numbers  $Re = 1.2 \times 10^4$  and  $Re = 1.5 \times 10^4$ . Each camera was equipped with a 105mm Micro Nikkor lens with a magnification of 0.085 in the four camera case and of 0.078 in the two camera case. The laser sheet was also horizontal ( $(x, y)$  plane) and entered the wind tunnel through a mirror positioned downstream in the wind tunnel test section (figure 1b). The f-stop was adjusted to 8 to get particle images of 1.7 pixels. The fields of view of consecutive cameras were adjusted to have a common region

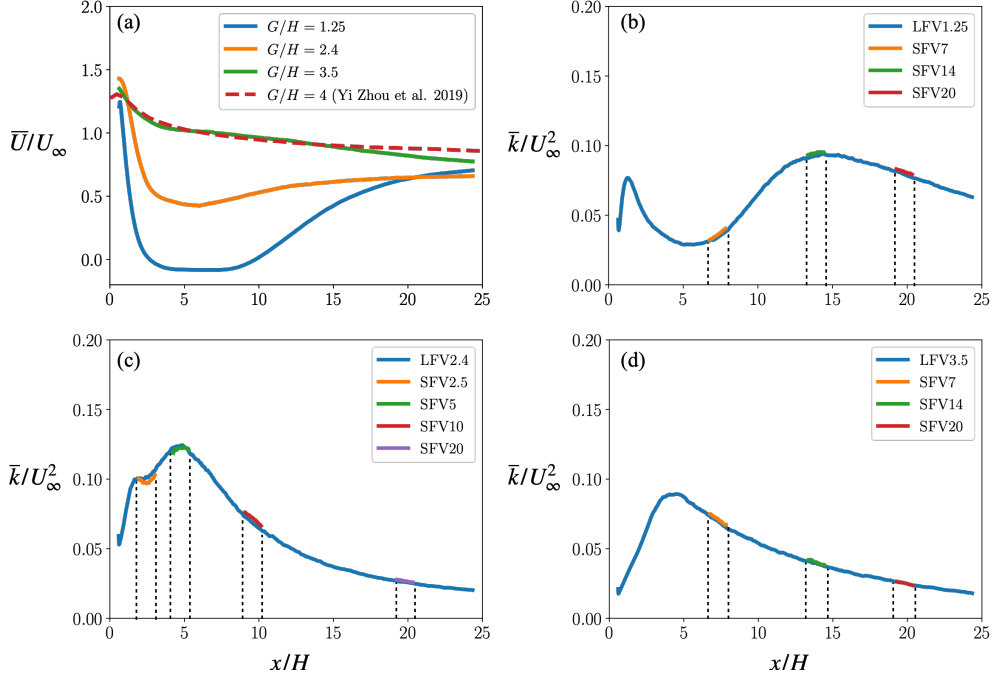


Figure 3: (a) Streamwise profiles of the normalised mean streamwise velocity  $\bar{U}/U_\infty$  along the wake centerline ( $y/H = 0$ ) for different gap ratios. The solid lines are from the LFMV measurements and the dashed line is from the DNS of Zhou *et al.* (2019). (b-d) Streamwise profiles of turbulent kinetic energy along the centreline taken from LFMV and SFVMV measurements at  $Re = 1.0 \times 10^4$ . Each plot corresponds to one value of  $G/H$ : (b)  $G/H = 1.25$ , (c)  $G/H = 2.4$ , (d)  $G/H = 3.5$ . The vertical dashed lines stand for the upstream and downstream boundaries of each SFVMV.

of 2cm to allow estimation of the level of uncertainty. Details of the LFMV measurements are listed in table 2.

For both SFVMV and LFMV measurements, the PIV delays were adjusted to have a maximum displacement of 12 pixels, and the acquisition frequency was 5Hz for SFVMV and 4 Hz for LFMV to ensure uncorrelated sample. 20,000 velocity fields were captured for each measurement. The seeding was carried out using Poly-Ethylene Glycol particles. The diameter of the particles was about  $1\mu\text{m}$  and the concentration was adjusted to have a number of particles per pixel of 0.04. The PIV analysis was carried out using an in-house software developed on a MatPIV basis. It is multi-pass and multi-grid (Willert & Gharib 1991; Soria 1996) and completes its analysis by image deformation (Scarano 2001; Lecordier & Trinite 2004) and a final  $24 \times 24$  pixel interrogation window, with about 58% overlap, which corresponds to  $312\mu\text{m}$  interrogation window for the SFVMV and about 1.6 mm for the LFMV.

The spatial resolution of the SFVMV measurements is important for a reliable estimation of  $\bar{\epsilon}$ . The ratio of the interrogation window size ( $\Delta d$ ) to the Kolmogorov length scale  $\eta \equiv (\nu^3/\bar{\epsilon})^{1/4}$  for all the measured positions along the wake centerline is displayed in figure 2. It should be noted that for each gap ratio at a particular position, only the case with the highest  $Re$  is shown. The ratio  $\Delta d/\eta$  varies from 4.5 in the nearest position (SFVMV2.5) to 2.5 in the farthest position (SFVMV20). For most positions,  $\Delta d/\eta$  is generally below 4, except for the very nearest one. It has been shown that a PIV resolution of  $\Delta d/\eta \leq 5$  can provide an estimation of the

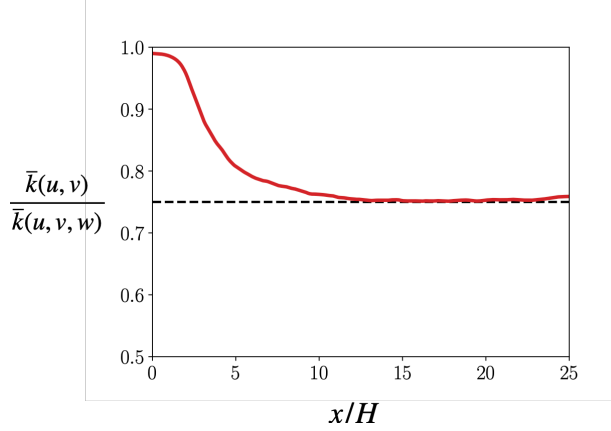


Figure 4: Ratio of  $(\overline{u^2} + \overline{v^2})/2$  to  $(\overline{u^2} + \overline{v^2} + \overline{w^2})/2$  from the DNS data (courtesy of Dr Yi Zhou of Nanjing University of Science and Technology) of Zhou *et al.* (2019).  $Re = 2500$ ,  $G/H = 4$  and  $y/H = 0$ .

energy dissipation rate with an uncertainty of less than 30% (e.g. Lavoie *et al.* 2007; Tokgoz *et al.* 2012). Therefore, the spatial resolution in the present study should provide a reliable estimation of the energy dissipation rate, especially for  $x/H \geq 4$ .

We close this section with two comparisons: a comparison of the streamwise mean flow velocity obtained from one of our LFVs and the streamwise mean flow velocity obtained for the same type of flow by the direct numerical simulation (DNS) of Zhou *et al.* (2019) (figure 3a); and a comparison of the turbulent kinetic energies obtained from our SFV and LFV measurements (figure 3b,c,d). The streamwise profile of the normalised time-averaged streamwise velocity  $\overline{U}/U_\infty$  along the geometric centerline for gap ratio  $G/H = 4$  obtained by Zhou *et al.* (2019) at  $Re = 2500$  agrees well with the present measurements for  $G/H = 3.5$  at  $Re = 1.0 \times 10^4$ .

Figure 3a also illustrates the very significant differences in mean flow profiles between the three gap ratios that we consider here. Equally significant inhomogeneity differences are also manifest in the streamwise turbulence kinetic energy profiles in Figure 3b,c,d. These are clearly flows with very different inhomogeneity structures.

Following Kolář *et al.* (1997), the turbulent kinetic energy  $\bar{k}$  is estimated from  $(\overline{u^2} + \overline{v^2})/2$  as our PIV does not provide access to the spanwise velocity fluctuation component  $w$ . In figure 4 we plot a comparison between  $(\overline{u^2} + \overline{v^2})/2$  and  $(\overline{u^2} + \overline{v^2} + \overline{w^2})/2$  using the DNS data that Zhou *et al.* (2019) obtained for a turbulent flow generated by two side-by-side square prisms with  $G/H = 4$  and a global Reynolds number of  $Re = 2500$ . This comparison suggests that  $(\overline{u^2} + \overline{v^2})/2$  captures about 75% to 80% of  $(\overline{u^2} + \overline{v^2} + \overline{w^2})/2$  for  $x/H \geq 5$ . More importantly for our scaling study of section 4, the ratio of  $(\overline{u^2} + \overline{v^2})/2$  to  $(\overline{u^2} + \overline{v^2} + \overline{w^2})/2$  remains about constant in this  $x/H$  range. (We could have made an assumption of axisymmetry to estimate  $(\overline{u^2} + \overline{v^2} + \overline{w^2})/2$  from  $\overline{u^2}/2 + \overline{v^2}$  but we do not expect such an estimation to either invalidate our choice of turbulent kinetic energy surrogate or significantly change this paper's conclusions because  $\overline{u^2}/\overline{v^2}$  is close to 1 in our SFVs for  $x/H \geq 7$  when  $G/H = 2.4$  and 3.5.)

Finally, figure 3b,c,d compares the kinetic energies  $\bar{k} = (\overline{u^2} + \overline{v^2})/2$  obtained from the LFV measurements with the kinetic energies  $\bar{k} = (\overline{u^2} + \overline{v^2})/2$  obtained from the denoised SFV measurements and shows that the two independent  $\bar{k}$  measurements overlap for all  $G/H$  cases and in all SFV positions.



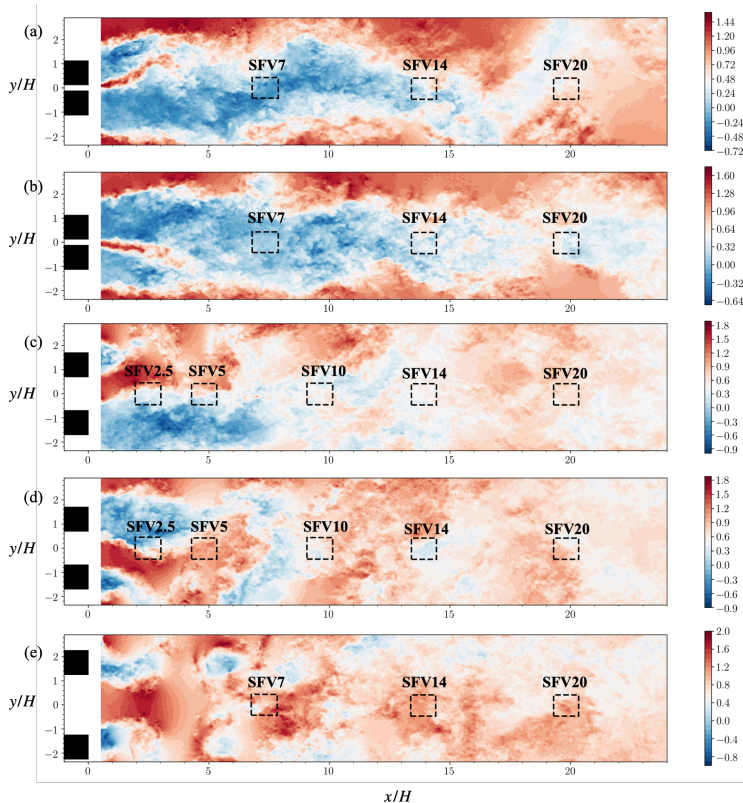


Figure 5: Examples of flow patterns of normalised instantaneous streamwise velocity  $U/U_\infty$  in the wake of the two prisms (filled squares) at  $Re = 1.0 \times 10^4$ . (a, b)  $G/H = 1.25$ , (c, d) 2.4, (e) 3.5. The positions of SFVs for each gap ratio are also displayed with dashed squares.

### 3. The velocity, turbulent kinetic energy and integral length scale

Figure 3 gives some initial appreciation of the qualitative and quantitative differences in inhomogeneity structure of our three flows. In this section we document the qualitatively different dynamics and flow types as well as the different types of statistical inhomogeneity between the three flows in the horizontal  $(x, y)$  plane. We look at planar fields of instantaneous streamwise and cross-stream velocities  $(U, V)$ , time-averaged streamwise and cross-stream velocities  $(\bar{U}, \bar{V})$  and turbulent kinetic energy  $\bar{k}$  in subsection 3.1. In subsection 3.2 we report on the variation of the integral length scale in the  $(x, y)$  plane. The results in this section are from our LFV measurements.

#### 3.1. Velocity and turbulent kinetic energy

We start with instantaneous velocity fields. Figure 5 shows distinctly different instantaneous streamwise velocity fields for the three gap ratios (i.e.  $G/H = 1.25, 2.4$  and  $3.5$ ) and confirms the three different typical flow patterns mentioned in this paper's introduction: 'single-bluff-body regime' for  $G/H = 1.25$ , 'asymmetric wake regime' for  $G/H = 2.4$  and 'couple-street regime' for  $G/H = 3.5$ . The solid black squares in the plots of figure 5 (and some subsequent figures) represent the square prisms which generate the wake. The empty dashed squares are the positions of the SFVs.

In the case  $G/H = 1.25$  (figure 5a, b), the two prisms are so close that the shear layers

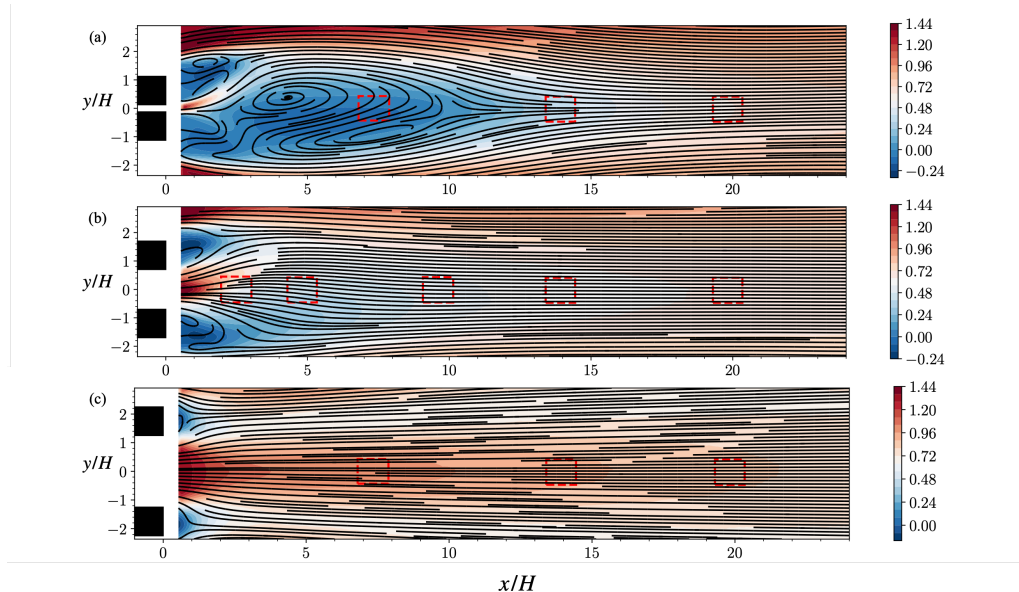


Figure 6: Planar mean flows for the three different gap ratios at  $Re = 1.0 \times 10^4$ . The solid lines represent mean flow streamlines of mean velocities  $(\bar{U}, \bar{V})$  and the colour-filled iso-contours stand for  $\bar{U}/U_\infty$ . (a)  $G/H = 1.25$ , (b) 2.4, (c) 3.5.

on the outer side of each prism develop into a single-body-like wake, even though a small gap flow persists between the two prisms. This small gap flow breaks the symmetry and randomly flips between being biased towards one prism (figure 5a) to the other (figure 5b) with time intervals which can be as long as about 10 minutes, i.e. an order of  $10^5 H/U_\infty$ . Such bi-stability with such long flip-times results in an asymmetric time-average mean flow  $(\bar{U}, \bar{V})$  even though the time-average is taken over 20,000 images taken at 4Hz, i.e. about 83 minutes (section 2). The mean gap flow for our statistics turns out to be biased “upwards” (figure 6a) instead of being straight as would be expected from a symmetric inlet condition. The momentum of the narrow gap flow is small and very sensitive to perturbations in the flow (e.g. Ishigai & Nishikawa 1975; Alam & Zhou 2013), and it is impossible to ensure perfect symmetry of perturbations during measurements.

The gap flow between the prisms remains biased in the case  $G/H = 2.4$  (figure 5c, d), but it is stronger and therefore interacts with the shear layers from the outer sides of the prisms causing the wake of that particular prism towards which the gap flow is biased to be displaced in the same direction. As the gap flow has now a larger momentum than in the  $G/H = 1.25$  case, it more often randomly flips from one side to the other (figure 5 c & d). Time intervals can now be as long as about 2 minutes, i.e. an order of  $10^4 H/U_\infty$ . As a result, the time-average flow is also asymmetric for  $G/H = 2.4$  (figure 6b) but less so than for  $G/H = 1.25$ .

As  $G/H$  increases to 3.5 (figure 5e), the gap flow between the prisms is no longer biased and each prism forms its own vortex street so that the whole wake results from the interaction between the two symmetrical vortex streets. The mean flow is now symmetric (figure 6c) and the flow between the prisms has a larger mean velocity than the flow directly downstream of the prisms.

For  $G/H = 1.25$  (figure 6a), the mean flow streamlines reveal a large-scale recirculation region downstream of the prisms, resulting in a mean streamwise velocity deficit in the central

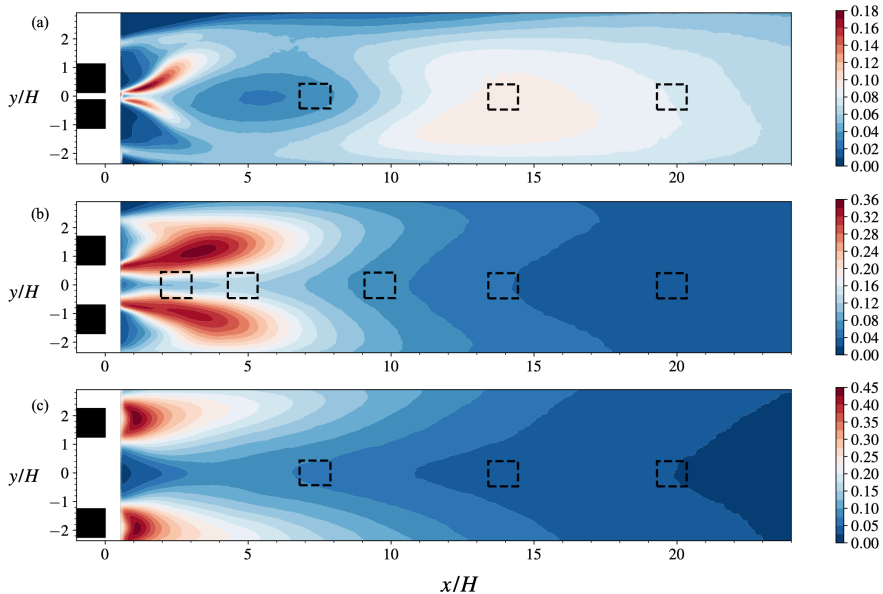


Figure 7: Spatial distribution of normalised turbulent kinetic energy  $\bar{k}/U_\infty^2$  for different gap ratios at  $Re = 1.0 \times 10^4$ . (a)  $G/H = 1.25$ , (b) 2.4, (c) 3.5.

region of this wake. The mean flow in the  $G/H = 2.4$  case (figure 6b) is a combination of the characteristics of  $G/H = 1.25$  and  $G/H = 3.5$ . Clearly the three different flow cases have significantly different mean flow characteristics, as well as different dynamics.

Consistent with the different instantaneous and mean planar velocities of the three  $G/H$  flow cases, their turbulent kinetic energy  $\bar{k}$  also exhibits distinct features as shown in figure 7. The shear layers from the prisms have high kinetic energy in all three cases. It is worth noting, though, that for  $G/H = 1.25$  (figure 7a) and  $G/H = 2.4$  (figure 7b), the energies of the inner side shear layers are much higher than the energies on the outer side. On the contrary, for  $G/H = 3.5$  (figure 7c), the wake behind each individual prism is more symmetric and the shear layers from either side have similar levels of kinetic energy. It is interesting to see that there is a large-scale low energy region in the  $G/H = 1.25$  flow (figure 7a), upstream of where the kinetic energy peaks, corresponding to the large recirculation region in the mean flow (figure 6a). A break of symmetry due to bi-stability is manifest in the turbulent energy map of the  $G/H = 1.25$  flow (figure 7a), but for the other two cases (figure 7b,c) the turbulent energy is symmetrically distributed with respect to the centerline ( $y = 0$ ) and decays monotonically downstream after reaching a maximum at a much shorter streamwise distance than for the  $G/H = 1.25$  flow (see also figure 3b,c,d).

### 3.2. Integral length scale

Integral length scales are obtained from the LFV measurements with the four-camera PIV system. The integral scales we calculate are obtained from

$$L_i(x, y) \equiv \int_0^{r_0} R_i(x, y, r_x) dr_x \quad \text{with} \quad R_i = \frac{\overline{u_i(x, y)u_i(x + r_x, y)}}{\sqrt{u_i(x, y)^2} \sqrt{u_i(x + r_x, y)^2}} \quad (3.1)$$

where  $r_x$  is the streamwise separation between two points in the horizontal plane,  $r_0$  is the value of  $r$  where the two-point auto-correlation coefficient  $R_i$  first crosses zero (figure 8),

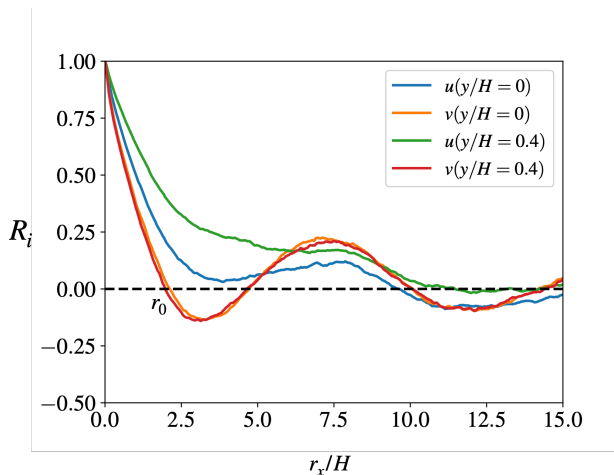


Figure 8: Streamwise two-point auto-correlation coefficients  $R_i$  for  $i = 1, 2$  with  $u_1 \equiv u$  and  $u_2 \equiv v$  at two different cross-stream positions,  $(x/H = 5, y/H = 0)$  and  $(x/H = 5, y/H = 0.4)$ , in the case of  $G/H = 2.4$  and  $Re = 1.0 \times 10^4$ .

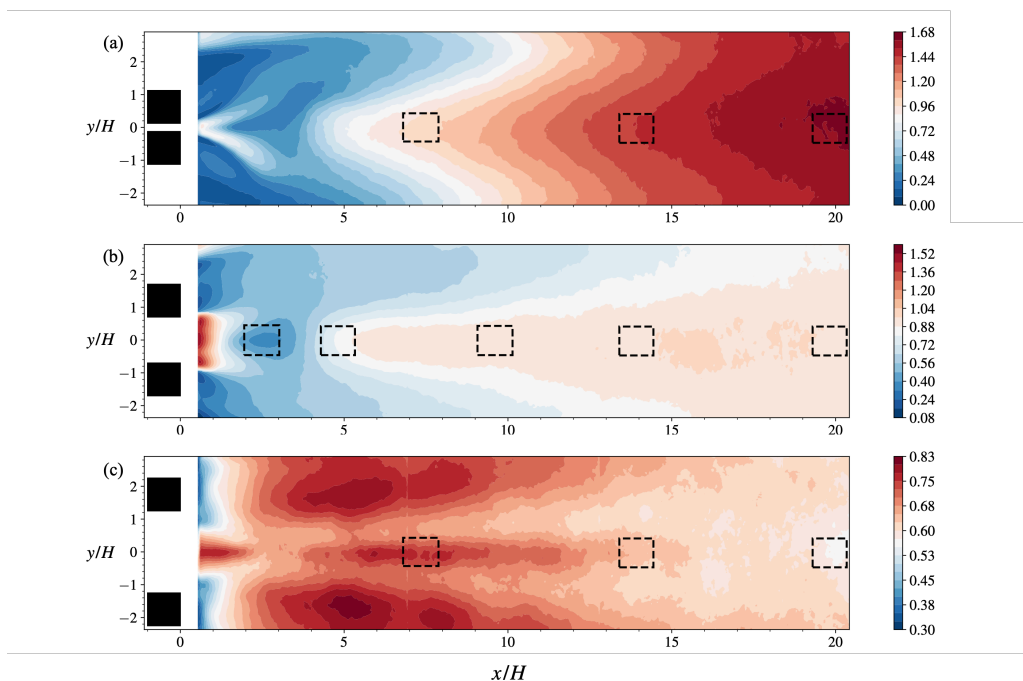


Figure 9: Map of normalised integral length scales  $L/H$  in the  $(x, y)$  plane for each gap ratio at  $Re = 1.0 \times 10^4$ . (a)  $G/H = 1.25$ , (b) 2.4, (c) 3.5.

where  $i = 1, 2$  with  $u_1 \equiv u$  and  $u_2 \equiv v$  (there is of course no summation over the index  $i$ , and the overbar is the average over time).

Figure 8 compares the two-point auto-correlation coefficient  $R_1$  for  $u$  at two lateral positions ( $y/H = 0$  and  $0.4$ ) with  $R_2$  for  $v$  in the case of  $G/H = 2.4$  and  $Re = 1.0 \times 10^4$ . (The other cases produce similar auto-correlations.) It can be seen from this figure that  $R_2$  for  $v$  decreases quickly and varies periodically with  $r_x$ , which reflects the periodic large-scale vortices in

the flow. It can also be seen in figure 8 that  $R_1$  for  $u$  reaches its first zero-crossing at a separation  $r_x$  close to  $10H$  which is a very long distance, well above the length scale of the energy-containing vortices which is commensurate with  $H$  and the local width of the wake(s) (Hayakawa & Hussain 1989; Zhou *et al.* 2002). A similar observation of long range streamwise auto-correlations of  $u$  was made by Chen *et al.* (2020) in the wake of a single prism reflecting long streaky structures formed between the energy containing vortices. On the basis of these considerations, we adopt the integral length scale  $L \equiv L_2$  of the cross-stream fluctuations  $v$  in the definition of  $C_\epsilon$  in our study of how  $C_\epsilon$  and  $Re_\lambda$  may relate to each other.

The integral length scale  $L \equiv L_2$  for all three gap ratios at  $Re = 1.0 \times 10^4$  is shown in figure 9. For  $G/H = 1.25$  (figure 9a),  $L(x, y)$  increases gradually as flow develops downstream, and is larger near the wake centerline than in the ambient region, which is similar to the streamwise evolution of the integral length scale in the wake of a single cylinder (e.g. Beaulac & Mydlarski 2004).  $L(x, y)$  at  $G/H = 2.4$  (figure 9b) displays a distribution resembling that of  $G/H = 1.25$ , except that  $L(x, y)$  is much larger in the gap flow region for  $G/H = 2.4$  than for  $G/H = 1.25$ .  $L(x, y)$  for  $G/H = 3.5$  (figure 9c) differs from the streamwise increasing  $L(x, y)$  for  $G/H = 2.4$  and  $G/H = 1.25$ : it grows downstream of the prisms, reaches maxima, and decays downstream of these maxima.  $L(x, y)$  in the  $G/H = 3.5$  case is generally smaller than  $L(x, y)$  in the  $G/H = 2.4$  and  $G/H = 1.25$  cases. The qualitatively different integral scale maps for our three gap ratios are consistent with the observation that the vortex formation lengths for  $G/H = 1.25$  and  $G/H = 2.4$  are much larger than for  $G/H = 3.5$  (e.g. Alam *et al.* 2011), since the integral length scale physically reflects the size of the energy-containing vortices in the flow field.

This section has demonstrated the significant qualitative differences in the dynamics, large scale features and inhomogeneity structures of the three different gap flows considered in this study. Instantaneous velocities, mean flow velocities, turbulent kinetic energy and integral length scale values and maps are indeed very different in the three flows. We can therefore use these three flows to study potential cross-stream relations between  $C_\epsilon$  and  $Re_\lambda$  in qualitatively different flow contexts, both with and without changing inlet Reynolds number. It is even possible to see whether any spatial relation that we may find between  $C_\epsilon$  and  $Re_\lambda$  is sensitive to the asymmetry which can be imposed by bi-stability.

## 4. Turbulent energy dissipation rate scaling

In this section, we examine the scalings of the energy dissipation rate by looking at different positions in different wake flows generated by side-by-side prisms with different gap ratios and different inlet/global Reynolds numbers.

### 4.1. Scaling of $C_\epsilon$ with all scales of motions

Figure 10 shows examples of isocontours of turbulent kinetic energy  $\bar{k}/U_\infty^2$ , integral length scale  $L/H$  and energy dissipation rate  $\bar{\epsilon}$  at different streamwise positions of the same flow. The main point we make with these examples taken from the  $G/H = 2.4$  flow is that inhomogeneity is also present in the small fields of view (SFV) for all the three quantities plotted. The same point can be made with similar plots for our two other  $G/H$  flows but we omit them for economy of space.

The small field of view inhomogeneities are consistent with the large field of view inhomogeneities: the kinetic energy varies mostly in the cross-stream direction inside SFV2.5 (figure 10a) and SFV5 (figure 10b) and decays in the streamwise direction within SFV10 (figure 10c) and SFV20 (figure 10d), which is consistent with the spatial evolution of the

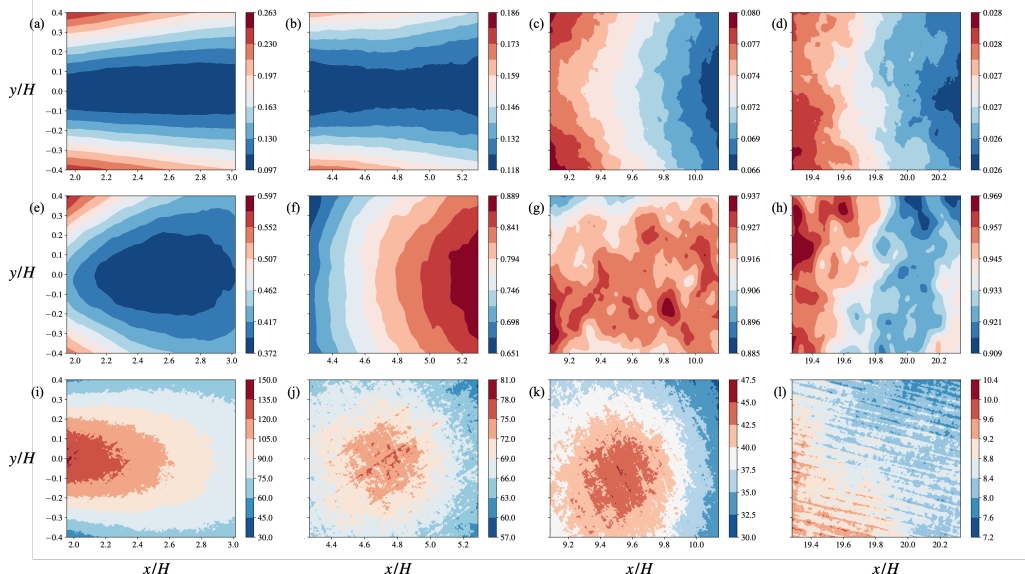


Figure 10: Isocontours of (a - d) turbulent kinetic energy  $\bar{k}/U_\infty^2$ , (e - h) integral scale  $L/H$ , and (i - l) energy dissipation rate  $\bar{\epsilon}$  in the SFVs of the  $G/H = 2.4$  flow at  $Re = 1.0 \times 10^4$ . (a, e, i): SFV2.5; (b, f, j): SFV5; (c, g, k): SFV10; (d, h, l): SFV20.

kinetic energy in the LFV of the same flow case (figure 7b). The integral length scale (figure 10e-h) at each  $(x, y)$  location within the SFVs is obtained by interpolation of the result of the LFV measurement (figure 9b) and is therefore consistent with it by construction. The turbulence dissipation rate  $\bar{\epsilon}$  is also very inhomogeneous within the SFVs (figure 10i-l) and is even slightly asymmetrically distributed in SFV10 and SFV20, a remnant signature of bistability even though the time average was taken over 20,000 images taken at 5Hz for 67 mins (section 2). As expected, this asymmetry is even stronger in the  $G/H = 1.25$  case but is absent in the  $G/H = 3.5$  case (not shown here for economy of space). All three quantities show a tendency towards homogeneity with increasing distance downstream, particularly in the cross-stream direction, and most notably within SFV20.

Using our measured values of  $\bar{k}$ ,  $L$  and  $\bar{\epsilon}$  we compute the normalised dissipation rate  $C_\epsilon \equiv \bar{\epsilon}L/\mathcal{U}^3$  and the local Taylor length-based Reynolds number  $Re_\lambda \equiv \lambda\mathcal{U}/\nu$  where  $\lambda \equiv (15\nu\mathcal{U}^2/\bar{\epsilon})^{1/2}$  and  $\mathcal{U} = (2/3\bar{k})^{1/2}$ . As we are interested in cross-stream profiles, we calculate streamwise-averaged values of  $C_\epsilon$  and  $Re_\lambda$  within each SFV, denoted respectively  $\langle C_\epsilon \rangle(y)$  and  $\langle Re_\lambda \rangle(y)$ , which we plot as functions of  $y/H$  in Figure 11 in the nearest and furthest SFVs for all three gap ratios  $G/H$ . The global Reynolds number is the same in figures 10 and 11, namely  $Re = 1.0 \times 10^4$ , but our conclusions from these figures do not change for the different values of  $Re$  that we tried.

It is evident from figure 11 that  $\langle C_\epsilon \rangle$  increases when  $\langle Re_\lambda \rangle$  decreases and vice versa. This inverse relation between  $\langle C_\epsilon \rangle$  and  $\langle Re_\lambda \rangle$  holds for all gap ratios, all SFVs and all values of  $Re$  that we tried even though the  $y$ -dependencies of  $\langle C_\epsilon \rangle$  and of  $\langle Re_\lambda \rangle$ , and even the very ranges of  $\langle C_\epsilon \rangle$  and  $\langle Re_\lambda \rangle$  values, vary from case to case. We therefore have the beginnings of an answer to the two questions we posed in the introduction: it appears that there is indeed a relation between  $\langle C_\epsilon \rangle$  and  $\langle Re_\lambda \rangle$  in the transverse/cross-stream direction and that this relation resembles qualitatively the non-equilibrium/non-stationarity dissipation scaling (1.2) in that it is an inverse relation between  $\langle C_\epsilon \rangle$  and  $\langle Re_\lambda \rangle$  irrespective of gap ratio, position of SFV

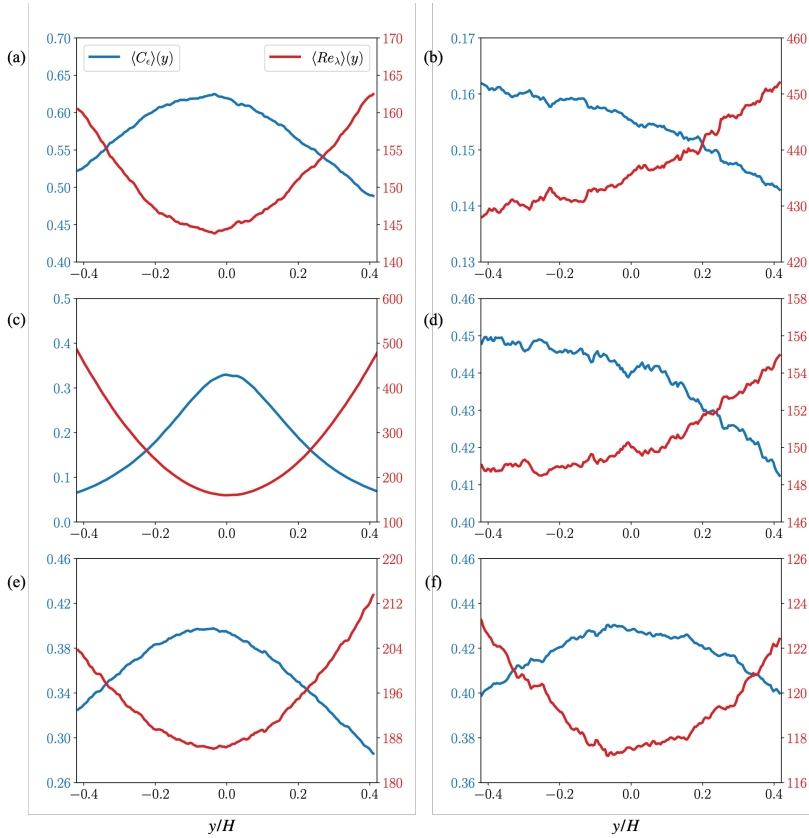


Figure 11: The lateral distributions of streamwise averaged non-dimensional dissipation rate  $\langle C_\epsilon \rangle(y)$  and turbulent Reynolds number  $\langle Re_\lambda \rangle(y)$  for different SFVs corresponding to the three gap ratios at  $Re = 1.0 \times 10^4$ . (a)  $G/H = 1.25$ , SFV7, (b) 1.25, SFV20; (c) 2.4, SFV2.5, (d) 2.4, SFV20; (e) 3.5, SFV7, and (f) 3.5, SFV20.

and global Reynolds number. It is worth noting that the dissipation asymmetry observed in figure 10k-l for  $G/H = 2.4$  is also present in SFV20 for  $G/H = 1.25$  but not for  $G/H = 3.5$  where bistability is absent, and it is also worth stressing that an inverse relation between  $\langle C_\epsilon \rangle$  and  $\langle Re_\lambda \rangle$  is observed both with and without asymmetry.

The Reynolds number  $Re_\lambda$  is not small in all  $G/H$  and SFV cases (see figure 11), and is generally between 100 and 500 after being averaged in the streamwise direction within each SFV (which actually reduces it). The relatively high Reynolds number nature of our turbulent flows and flow regions is also manifested by the presence of Kolmogorov-like close to  $2/3$  power law exponents for the streamwise second-order structure functions of both  $u$  and  $v$ , observed in all SFVs for all  $G/H$  values; see figure 12 where exponents more or less close to  $2/3$  appear more or less well-defined over a decade of range of scales bounded from below by  $\lambda$ .

For more insight into the inverse relation between  $C_\epsilon$  and  $Re_\lambda$  and a better comparison with the non-equilibrium/non-stationarity dissipation scaling (1.2), we look at scatter plots of  $C_\epsilon$  and  $Re_\lambda$ , see figure 13. Different scatter plots are for different  $G/H$  values and different SFVs, though we chose to plot those for the closest and furthest SFVs. The values of  $C_\epsilon$  and  $Re_\lambda$  in these scatter plots are from 20 evenly spaced  $x$  for each  $y$  within the corresponding SFV.

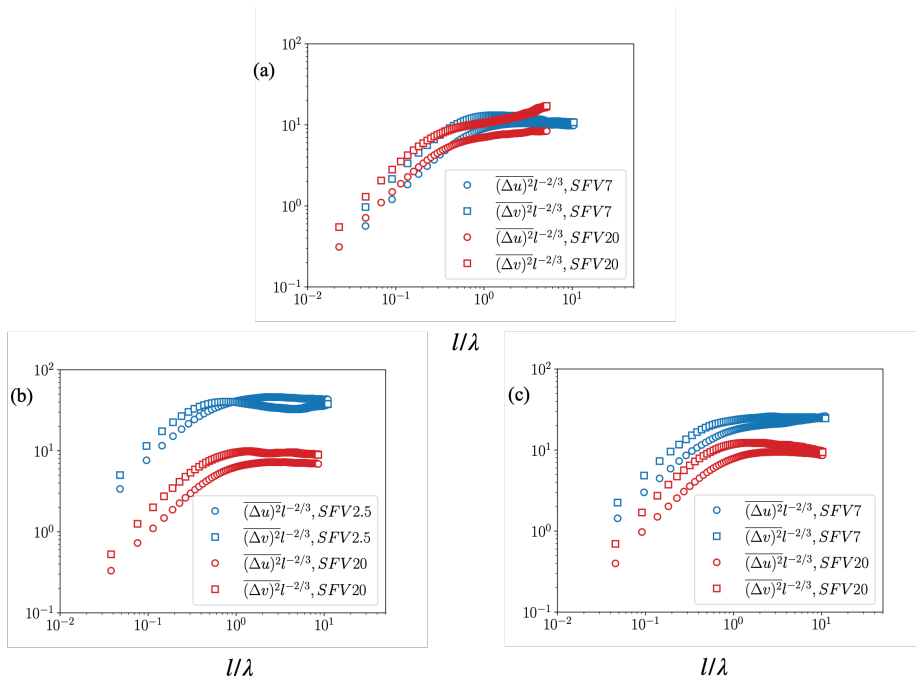


Figure 12: Compensated streamwise second-order structure functions

$(\Delta u)^2 = (u(x_0, y = 0) - u(x_0 + l, y = 0))^2$  and  $(\Delta v)^2 = (v(x_0, y = 0) - v(x_0 + l, y = 0))^2$  in different SFVs for all three gap ratios at  $Re = 1.0 \times 10^4$  ( $x_0$  is at a distance of about  $0.1H$  from the upstream boundary of the SFV). (a)  $G/H = 1.25$ , (b) 2.4, (c) 3.5.

These scatter plots confirm the inverse relation between  $C_\epsilon$  and  $Re_\lambda$  in the whole field of view rather than just between  $\langle C_\epsilon \rangle(y)$  and  $\langle Re_\lambda \rangle(y)$ . A best power law fit  $C_\epsilon \sim Re_\lambda^{-n}$  of the data is also given for each scatter plot. Power laws do appear to fit the data reasonably well in some cases but less so in other cases such as SFV7 for  $G/H = 1.25$  (figure 13a), SFV20 for  $G/H = 2.4$  (figure 13e) and SFV20 of  $G/H = 3.5$  (figure 13f). In those cases where the power law is an acceptable fit, the exponent  $n$  is not uniformly the same: for example  $n \approx 2.14$  for SFV20  $G/H = 1.25$  but  $n \approx 1.5$  for SFV2.5  $G/H = 2.4$ . Even though the spatial inhomogeneities of the turbulent kinetic energy, of the turbulence dissipation and of the integral length scale are such that  $C_\epsilon$  and  $Re_\lambda$  are anticorrelated in space, which is qualitatively similar to the non-equilibrium/non-stationarity dissipation scaling (1.2), there does not seem to be a well-defined universal power law relation between the spatial variabilities of  $C_\epsilon$  and  $Re_\lambda$ , which is unlike (1.2).

Alves Portela *et al.* (2018) reported that in the near wake of a single square prism, specifically  $x/H$  smaller than at least 10, the non-equilibrium dissipation scaling (1.2) is observed provided that the energy of the large-scale coherent structures is excluded. In the following sub-section we explore the hypothesis that the variability in the quality of the fit  $C_\epsilon \sim Re_\lambda^{-n}$  and of its exponent  $n$  may be due to the variability in large-scale structures present at different streamwise positions for different gap ratios  $G/H$ . We therefore explore the scalings of the spatial inhomogeneity of the turbulence dissipation when the coherent motions are removed.



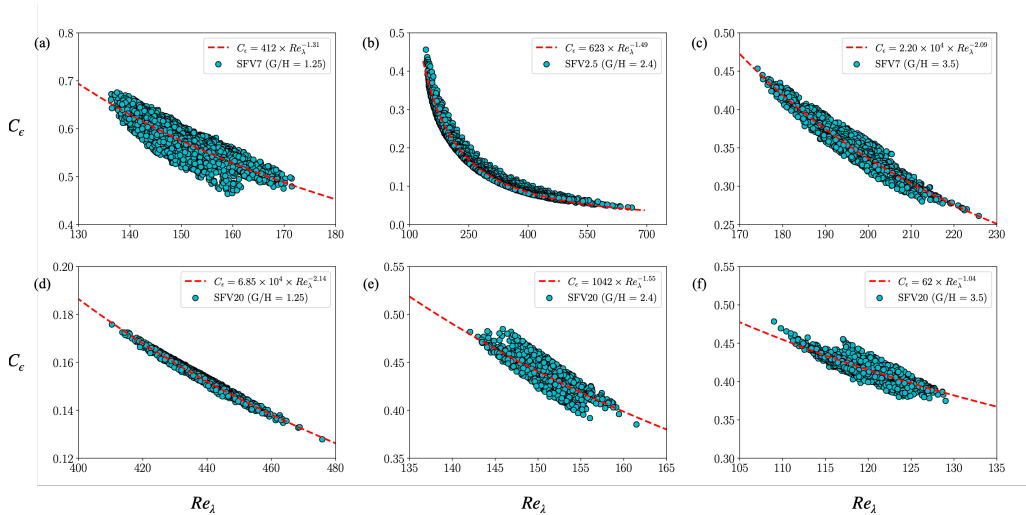


Figure 13: Scatter plots for  $C_\epsilon$  and  $Re_\lambda$  in different SFVs for the three gap ratios at  $Re = 1.0 \times 10^4$ . The red dashed line in each plot is fitted based on the least squares method for all the data points.

#### 4.2. Scaling of $C_\epsilon$ without the coherent motions

A snapshot POD method is used to decompose the flow velocity field into different orthogonal modes and then remove the most energetic coherent motions from the velocity field. A practical description of the POD method applied here is given in the Appendix. This method gives rise to a distribution of energies in different POD modes which we plot in figure 14 for all gap ratios and all SFVs at  $Re = 1.0 \times 10^4$ . It is interesting to see that the streamwise evolution (from one SFV to the next in the streamwise direction) of the energy of the first, most energetic, mode is consistent, for each  $G/H$ , with the streamwise evolution of the corresponding integral length scale (figure 9): the energy of the first mode in the  $G/H = 1.25$  case increases from SFV7 to SFV20 (figure 14a), while for  $G/H = 3.5$  the energy of the first mode energy decreases from SFV7 to SFV20 (figure 14c). For  $G/H = 2.4$  (figure 14b), the energy of the first mode decreases first from SFV2.5 to SFV5 and then increases further downstream. The corresponding integral length scale for each  $G/H$  varies in a similar way in the streamwise direction.

It can be seen from figure 14 that the first two modes stand out in terms of turbulent kinetic energy content. We therefore take the first two modes as representative of the coherent motions. We checked that the results of this subsection do not change appreciably if we were to define the coherent motions in terms of the first three modes.

In the following analysis, we divide the flow field into coherent motions, reconstructed using the first two modes in equation (5.6), and the remaining small-scale velocity field which is reconstructed using the rest of the modes in equation (5.6). We define the coherent turbulent energy  $\tilde{k}(x, y, t) = (\tilde{u}^2 + \tilde{v}^2)/2$  in terms of the streamwise and cross-stream coherent velocity fluctuations  $(\tilde{u}, \tilde{v})$  and the remaining turbulent kinetic energy  $k'(x, y, t) = (u'^2 + v'^2)/2$  in terms of the streamwise and cross-stream velocity fluctuations  $(u', v')$  in the remaining modes. Figure 15 shows, for  $G/H = 2.4$  and  $Re = 1.0 \times 10^4$ , maps of the time-averaged coherent turbulent energy,  $\overline{\tilde{k}}$  (figure 15a-d), of the time-averaged turbulent energy in the remaining motions,  $\overline{k'}$  (figure 15c-h) and of the time-averaged energy dissipation rate  $\overline{\epsilon'}$  in these remaining motions (figure 15i-l). It is worth noting, by comparing figures 15i-l and 10

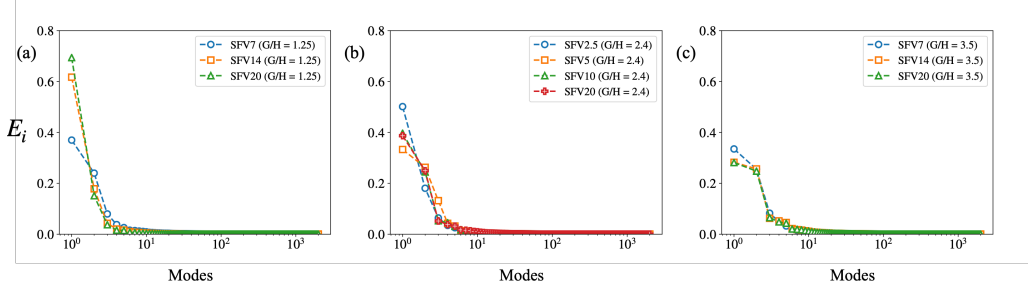


Figure 14: The distribution of turbulent energy among different POD modes,  $E_i$  given by (5.4), in different SFVs for different gap ratios at  $Re = 1.0 \times 10^4$ . (a)  $G/H = 1.25$ , (b) 2.5, (c) 3.5.

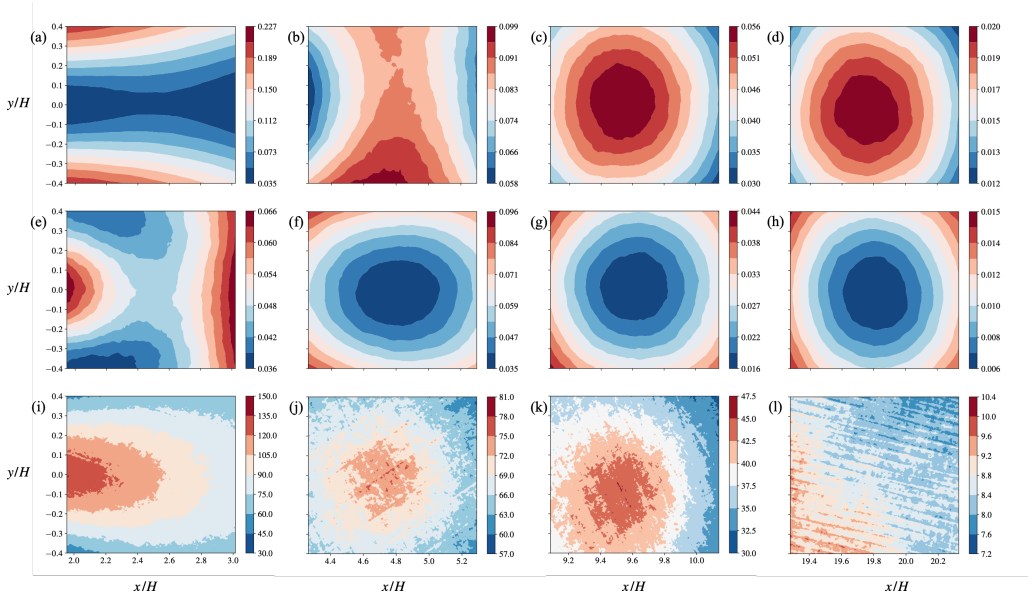


Figure 15: Isocontours of (a - d) coherent turbulent kinetic energy  $\overline{\overline{k}}/U_\infty^2$ , (e - h) remaining small-scale turbulent kinetic energy  $\overline{k'}/U_\infty^2$ , and (i - l) energy dissipation rate  $\overline{\epsilon'}$  in the SFVs corresponding to  $G/H = 2.4$  at  $Re = 1.0 \times 10^4$ . (a, e, i): SFV2.5, (b, f, j): SFV5, (c, g, k): SFV10, and (d, h, l): SFV20.

i-l, that the spatial distribution of  $\overline{\epsilon'}$  is effectively identical to that of  $\overline{\epsilon}$ . This correspondence is reasonable and validates our flow decomposition because the turbulent energy dissipation mainly occurs at the small scales.

Figure 15 demonstrates that the inhomogeneity remains present in the small fields of view with the decomposed fields but is now much more organised because of the extraction of the coherent motions. The coherent kinetic energy  $\overline{\overline{k}}$  is typically large where the small-scale kinetic energy  $\overline{k'}$  is small and vice versa. The sum of these two energies adds up to  $k$  plotted in figure 10a-d.

A better understanding of the opposite spatial distributions of  $\overline{\overline{k}}$  and  $\overline{k'}$  can be provided by representative instantaneous snapshots of  $\overline{\overline{k}}$ ,  $\overline{k'}$  and  $\epsilon'$ , shown in figure 16 for SFV2.5 and figure 17 for SFV5. The coherent motions are closer to the geometric centerline  $y = 0$  in the

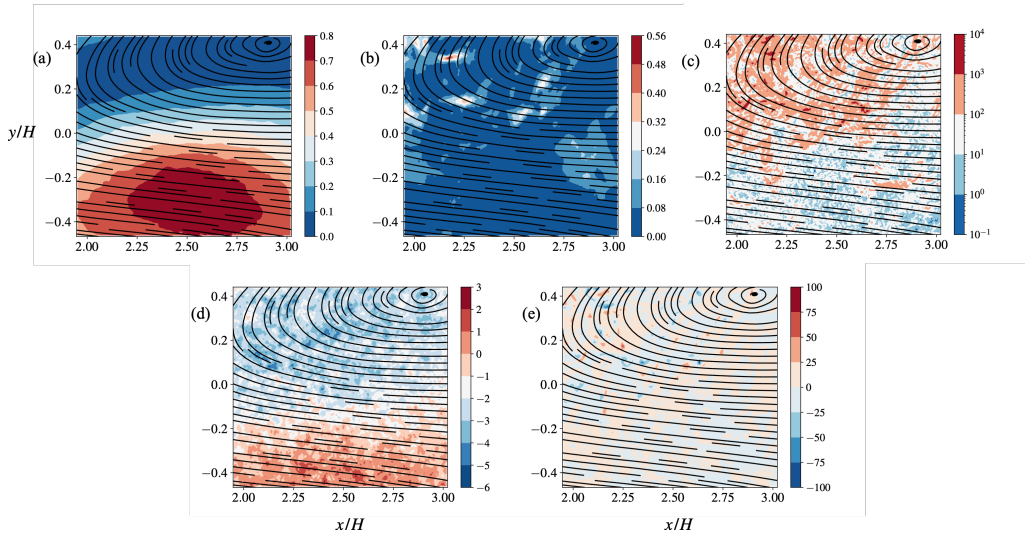


Figure 16: Instantaneous spatial distribution of (a)  $\tilde{k}$ , (b)  $k'k'$ , (c)  $e'\epsilon'$ , (d)  $\tilde{\omega}$ , and (e)  $\omega'\omega'$  with respect to the coherent vortex structure represented by solid line 2D streamlines in the case of SFV2.5 for  $G/H = 2.4$  and  $Re = 1.0 \times 10^4$ .

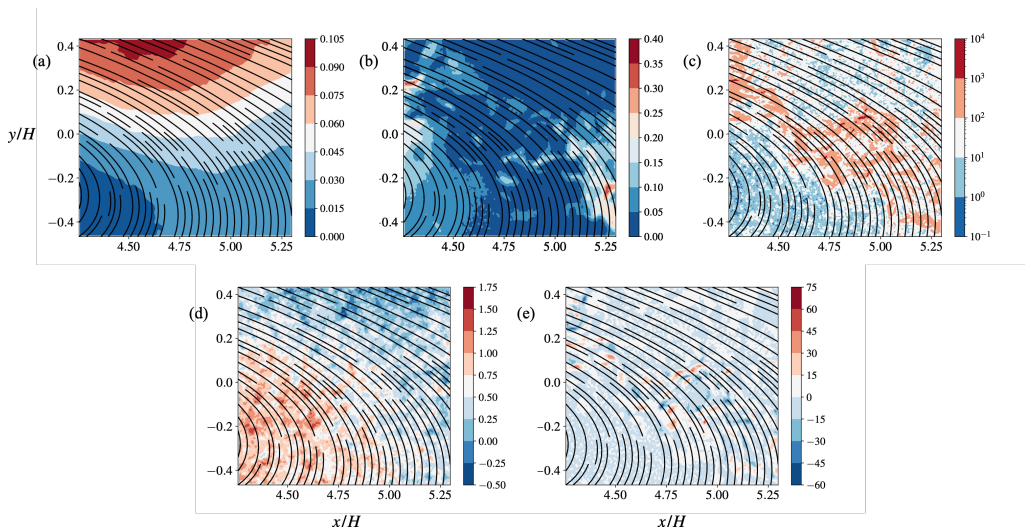


Figure 17: Instantaneous spatial distribution of (a)  $\tilde{k}$ , (b)  $k'k'$ , (c)  $e'\epsilon'$ , (d)  $\tilde{\omega}$ , and (e)  $\omega'\omega'$  with respect to the coherent vortex structure represented by solid line 2D streamlines in the case of SFV5 for  $G/H = 2.4$  and  $Re = 1.0 \times 10^4$ .

SFV2.5 and SFV5 measurements than in SFVs further downstream, and therefore easier to be identified in SFV2.5 and SFV5. The coherent motion streamlines obtained from  $(\tilde{u}, \tilde{v})$  and plotted as solid lines in figures 16 and 17 give a clear indication of where the centre of the large-scale coherent vortex is, particularly for SFV2.5, whereas this is not the case in SFVs further downstream. We checked that the instantaneous snapshots in figures 16 and 17 are quite typical, though the centre of the large-scale motion can be equally found on the positive or negative  $y$  sides.

A first striking observation in both figures 16 and 17 is that  $\tilde{k}$  (figures 16a, 17a) is high

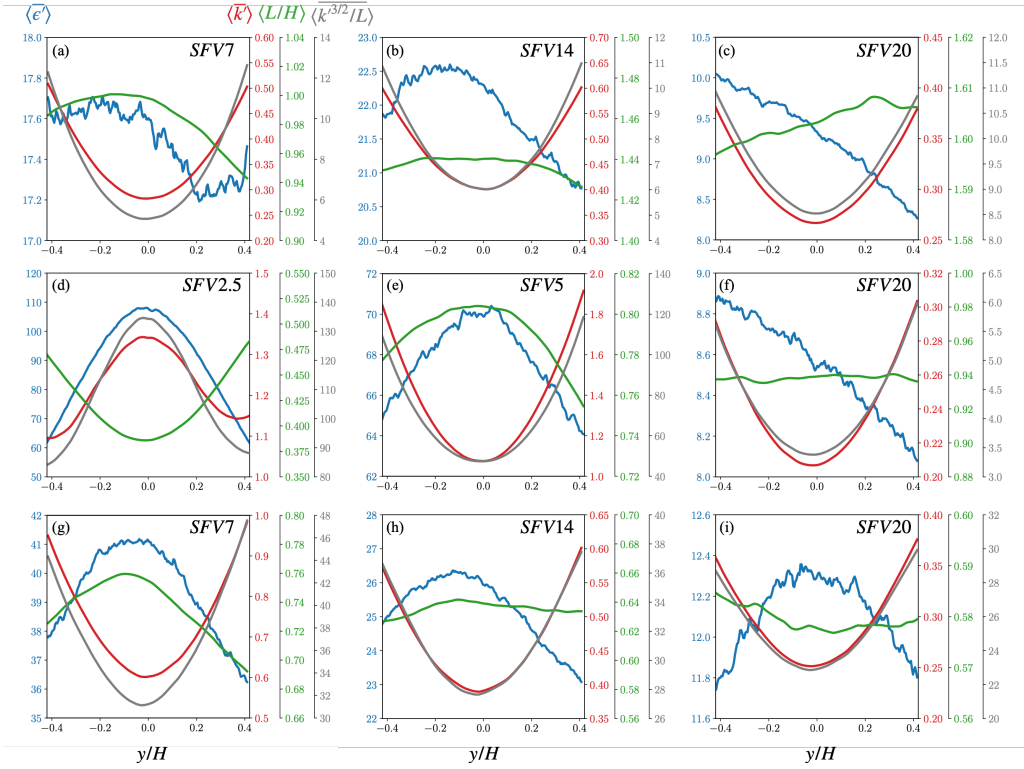


Figure 18: Streamwise-averaged energy dissipation rate  $\langle \epsilon' \rangle$  and turbulent kinetic energy  $\langle k' \rangle$  based on small-scale motions, integral scale  $\langle L \rangle$  and  $\langle k'^{3/2} \rangle / L$  for  $Re = 1.0 \times 10^4$  and different SFVs corresponding to (a - c)  $G/H = 1.25$ , (d - f) 2.4, and (g - i) 3.5.

far from the coherent motion's central region. The coherent vorticity  $\tilde{\omega} = \partial \tilde{v} / \partial x - \partial \tilde{u} / \partial y$  and the small-scale vorticity  $\omega' = \partial v' / \partial x - \partial u' / \partial y$  are also plotted in these snapshot figures. The maximum values of  $\tilde{k}$  are located near the boundary between the positive and negative coherent vorticity  $\tilde{\omega}$  (figures 16d and 17d). This observation is consistent with Zhou & Antonia (1993) and Chen *et al.* (2019) who reported that the coherent tangent velocity increases rapidly with increasing distance from vortex centre, reaching a maximum before decreasing slowly further away. The maximum coherent turbulent kinetic energy is indeed expected to be found at approximately the same distance away from the vortex center where the tangent velocity reaches its peak value. It is worth mentioning at this point that in SFVs further downstream, negative and positive coherent motions have their centres further away from the  $y = 0$  centreline so that their flow influence meets at the centre of such downstream SFVs thereby causing approximately circular  $\tilde{k}$  patterns. The time-average of these patterns is also circular as can be seen in figures 15c-d.

The second striking observation in figures 16 and 17 is that the higher values of  $k'$  (figures 16b, 17b) are concentrated relatively close to the coherent motion's central region. The same is true for  $\omega'$  (figures 16e, 17e) and the turbulent energy dissipation rate  $\epsilon'$  (figures 16c, 17c) which, like  $k'$ , are therefore dislocated from  $\tilde{k}$ . Chen *et al.* (2018) also found that the turbulent energy dissipation occurs mainly within the von Kármán vortices in the wake of a single cylinder. The spatial proximity between high  $k'$  and high  $\epsilon'$  values (as well as high  $\omega'$  values) is not unexpected since they are all closely associated with the small-scale

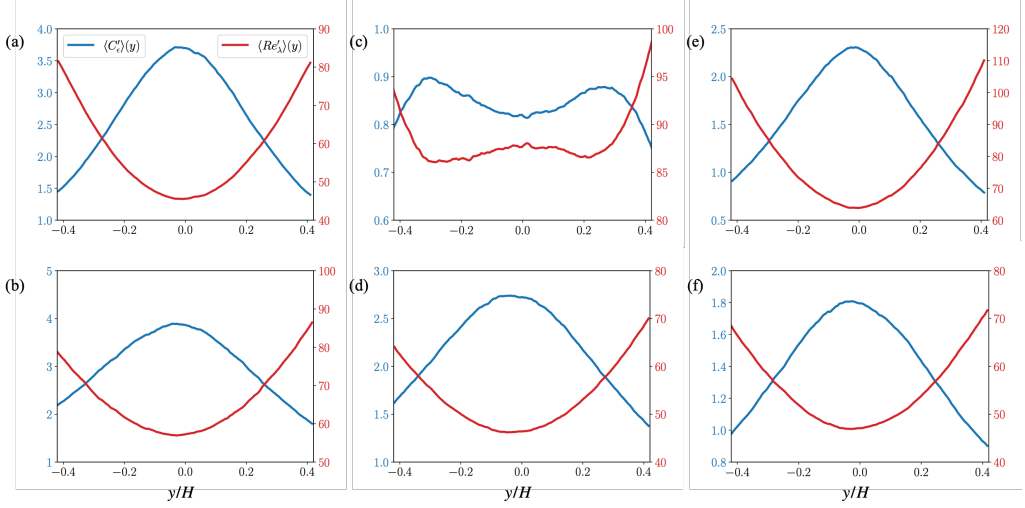


Figure 19: Streamwise-averaged non-dimensional energy dissipation rate  $\langle C'_\epsilon \rangle(y)$  and turbulent Reynolds number  $\langle Re'_\lambda \rangle(y)$  based on small-scale motions for  $Re = 1.0 \times 10^4$  and (a)  $G/H = 1.25$ , SFV7; (b) 1.25, SFV20; (c) 2.4, SFV2.5; (d) 2.4, SFV20; (e) 3.5, SFV7; (f) 3.5, SFV20.

fluctuations  $(u', v')$ . Note that, quite naturally, both  $k'$  and  $\epsilon'$  show much more intermittent spatial distribution than  $\bar{k}$ .

A closer look at figures 16 and 17 might suggest that there is no perfect collocation between  $k'$  and  $\epsilon'$  either and that high values of  $\epsilon'$  might more often occur around the centerline than high values of  $k'$ . In fact, this point about the centerline is not always true and the finer dislocation between  $k'$  and  $\epsilon'$ , which does indeed exist, is much subtler and is also non-universal. In figure 18 we plot time-averaged and streamwise-averaged turbulent energies and dissipations: to be precise, we plot  $\langle \bar{\epsilon}' \rangle$  and  $\langle \bar{k}' \rangle$  for all three  $G/H$  values and all SFVs except one (we omit the plots for SFV10  $G/H = 2.4$  because they look very similar to those for SFV7 in the  $G/H = 3.5$  case). The dislocation between  $k'$  and  $\epsilon'$  is evident in all SFVs except SFV2.5 for  $G/H = 2.4$  where both  $\langle \bar{\epsilon}' \rangle$  and  $\langle \bar{k}' \rangle$  are peaked at  $y = 0$ . It is clear that the statistical inhomogeneity of the turbulence is highly marked in all SFVs for all values of  $G/H$ . It is now the time to return to the main question posed in this paper: can the variety of cross-stream inhomogeneities in figure 18 be represented by a universal relation between  $C'_\epsilon \equiv \bar{\epsilon}' / (\bar{k}'^{3/2} / L)$  and  $Re'_\lambda \equiv \bar{k}'^{1/2} \lambda' / \nu$  where  $\lambda' \equiv (15\nu \bar{k}' / \bar{\epsilon}')^{1/2}$ ?

The first part of the answer to this question is provided in figure 19 where one can see that  $\langle C'_\epsilon \rangle(y)$  increases when  $\langle Re'_\lambda \rangle(y)$  decreases and vice versa, very much like  $\langle C_\epsilon \rangle(y)$  and  $\langle Re_\lambda \rangle(y)$  in figure 11 but with some different  $y$ -dependencies. Concerning the different  $y$ -dependencies, the  $y$ -asymmetry in some of the plots of figure 11 is absent in the plots of figure 19 presumably because of the strong symmetrising influence of the very symmetric distribution of  $\bar{k}'$  seen in figure 15f-h.

Once again, this inverse relation which now is between  $\langle C'_\epsilon \rangle(y)$  and  $\langle Re'_\lambda \rangle(y)$  holds for all gap ratios, all SFVs and all values of  $Re$  that we tried. Furthermore this qualitative inverse relation is universal as it holds for all the different  $y$ -dependencies in figure 18 where we plot  $\langle \bar{\epsilon}' \rangle(y)$ ,  $\langle \bar{k}' \rangle(y)$ ,  $\langle L/H \rangle(y)$  and  $\langle \bar{k}'^{3/2}/L \rangle(y)$  for all three  $G/H$  values and nearly all SFVs. These  $y$ -dependencies are in fact so widely different that it is impossible to make a simple argument for this inverse relation between  $\langle C'_\epsilon \rangle(y)$  and  $\langle Re'_\lambda \rangle(y)$  on the basis that

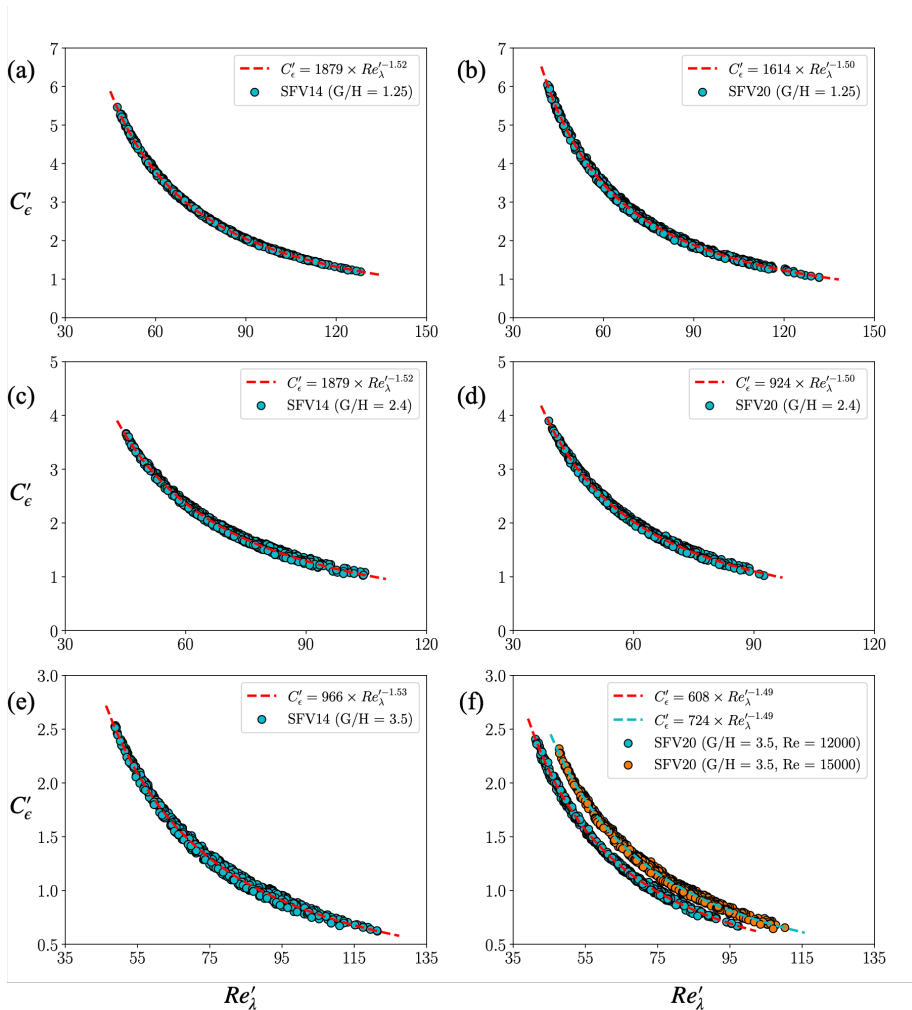


Figure 20: Scatter plots of  $C'_\epsilon$  and  $Re'_\lambda$  values in different SFVs for each gap ratio and for two inlet Reynolds numbers. (a - f)  $Re = 1.2 \times 10^4$  and (f)  $Re = 1.5 \times 10^4$ .

$C'_\epsilon \equiv \overline{\epsilon'} / (\overline{k'}^{3/2} / L)$  and  $Re'_\lambda \sim \overline{k'} / \sqrt{v\overline{\epsilon'}}$ . Indeed, if it was always the case that  $\langle \overline{\epsilon'} \rangle(y)$  increases or decreases when  $\langle \overline{k'} \rangle(y)$  decreases or increases and if the  $y$ -dependence of  $\langle L/H \rangle(y)$  was always weak, then the inverse relation between  $\langle C'_\epsilon \rangle(y)$  and  $\langle Re'_\lambda \rangle(y)$  could indeed be no more than a reflection of an inverse relation between  $\langle \overline{\epsilon'} \rangle(y)$  and  $\langle \overline{k'} \rangle(y)$ . However it is clear from figure 18 that this is not the case. The universal inverse relation between  $\langle C'_\epsilon \rangle(y)$  and  $\langle Re'_\lambda \rangle(y)$  holds for many different types of cross-stream inhomogeneity.

For a better comparison with the non-equilibrium/non-stationarity dissipation scaling (1.2) and for a more complete answer to the main question posed in this paper, we now look at scatter plots of  $C'_\epsilon$  and  $Re'_\lambda$ , see figure 20. Different scatter plots are for different  $G/H$  values and different SFVs, though we once again chose to plot those for the closest and furthest SFVs. The values of  $C'_\epsilon$  and  $Re'_\lambda$  in these scatter plots are from 20 evenly spaced values of  $x$  for each  $y$  within the corresponding SFV. These scatter plots confirm the inverse relation between  $C'_\epsilon$  and  $Re'_\lambda$  in the whole field of view rather just between  $\langle C'_\epsilon \rangle(y)$  and  $\langle Re'_\lambda \rangle(y)$ . A best power law fit  $C'_\epsilon \sim Re'^{-n}$  of the data is also given for each scatter plot. Power laws now

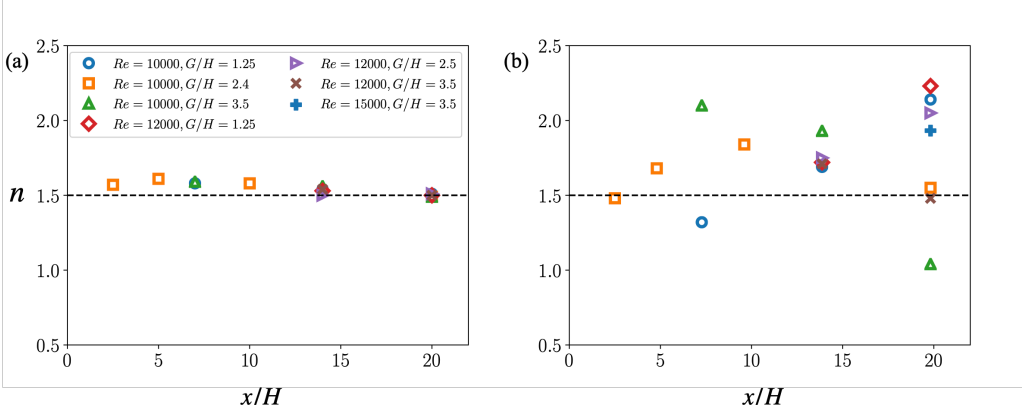


Figure 21: Scaling exponent  $n$  in (a)  $C'_\epsilon \sim Re'_\lambda^{-n}$  for the flow fields reconstructed based on random motions (POD modes 3 to 2000) and in (b)  $C_\epsilon \sim Re_\lambda^{-n}$  for the flow fields with coherent motions. The different values of  $x/H$  correspond to different SFVs.

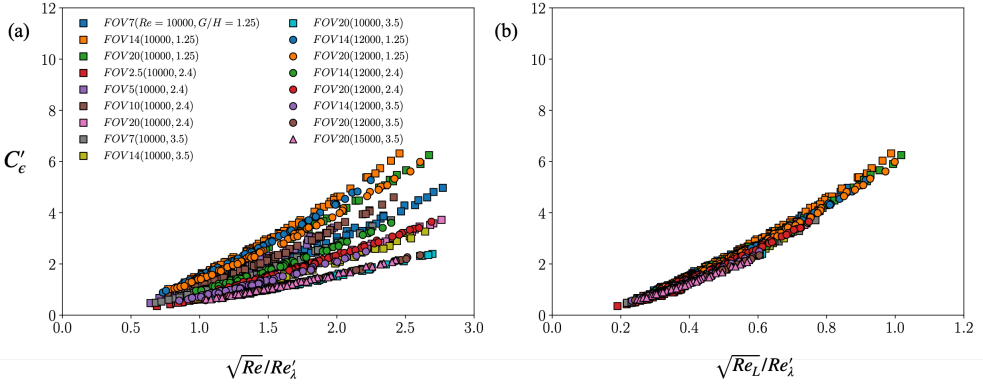


Figure 22: Comparison between two different choices of global Reynolds number for all the measured cases at different gap ratios and inlet Reynolds numbers. (a)  $C'_\epsilon$  versus  $\sqrt{Re}/Re'_\lambda$ , and (b)  $C'_\epsilon$  versus  $\sqrt{Re_L}/Re'_\lambda$  with  $Re_L \equiv \langle \sqrt{k'} \rangle_{xy} \langle L \rangle_{xy} / \nu$ .

appear to fit the data rather well in all cases and for all the global Reynolds numbers that we tried. There is in fact very little scatter in these scatter plots.

In figure 21 we plot the power law exponents  $n$  in  $C'_\epsilon \sim Re'_\lambda^{-n}$  for each case (different values of  $G/H$  and global Reynolds number  $Re$  and different SFVs) and compare them with the power law exponents obtained from best fits of the  $(C_\epsilon, Re_\lambda)$  scatter plots in figure 13 for each gap ratio. Quite remarkably, exponents very close to  $n = 1.5$  are returned universally for all  $C'_\epsilon \sim Re'_\lambda^{-n}$  fits, whereas the values of  $n$  returned for the  $C_\epsilon \sim Re_\lambda^{-n}$  fits in figure 13 range between  $n = 1$  and  $n = 2.3$ .

In spite of the wide variety and complexity of the spatial inhomogeneities of the turbulent flows considered here, the equally varied near-field ( $x \leq 20H$ ) inhomogeneities of the turbulent kinetic energy, of the turbulence dissipation and of the integral length scale are closely linked together by a simple universal relation,  $C'_\epsilon \sim Re'_\lambda^{-3/2}$ , once the large-scale coherent motions have been removed from the flow. The expectation that  $C'_\epsilon$  should be independent of viscosity at the sufficiently high Reynolds numbers of this paper's turbulent flows means that  $C'_\epsilon$  should also depend on a global Reynolds number, as is in fact the case

of the non-equilibrium/non-stationarity turbulence dissipation scaling (1.2). One may try  $C'_\epsilon \sim (\sqrt{Re}/Re'_\lambda)^{3/2}$  in terms of the global Reynolds number  $Re = U_\infty H/\nu$  but figure 22a shows that  $C'_\epsilon$  versus  $\sqrt{Re}/Re'_\lambda$  does not collapse all  $G/H$  and  $SFV$  cases. A careful look at figure 22a reveals, however, that for a given  $G/H$  and a given  $SFV$ ,  $C'_\epsilon$  versus  $\sqrt{Re}/Re'_\lambda$  does collapse different  $Re$  values. We therefore define a local global Reynolds number  $Re_L \equiv \langle \sqrt{k'} \rangle_{xy} \langle L \rangle_{xy} / \nu$  where  $\langle \dots \rangle_{xy}$  is an average over the entire  $SFV$  considered for a given  $G/H$ . Figure 22b shows that  $C'_\epsilon$  versus  $\sqrt{Re_L}/Re'_\lambda$  collapses all our data for all gap ratios,  $SFVs$  and global Reynolds numbers. Hence,

$$C'_\epsilon \sim (\sqrt{Re_L}/Re'_\lambda)^{3/2}. \quad (4.1)$$

We checked that this scaling is robust to moderate changes of the  $(x, y)$  range over which the average  $\langle \dots \rangle_{xy}$  is taken. However, further research is needed in the future to establish a priori ways of determining the proper spatial extent of this average, which may probably be of the order of the integral length-scale and/or a characteristic size of the large-scale coherent structures.

## 5. Conclusion

The scaling (4.1) is the main result of this paper. It describes how the variations along the cross-stream direction of the turbulent kinetic energy, the turbulent kinetic energy dissipation and the integral length scale are closely interlinked. This scaling holds for several streamwise positions in three significantly different turbulent flows and three different inlet Reynolds numbers. It shares clear qualitative similarities with the scaling  $C'_\epsilon \sim \sqrt{Re_G}/Re'_\lambda$  found along the streamwise direction of a planar turbulent near wake (Alves Portela *et al.* 2018), and also with the scaling  $C_\epsilon \sim \sqrt{Re_G}/Re_\lambda$  characterising variations in time of periodic turbulence (Goto & Vassilicos 2015, 2016*a,b*) and variations along the streamwise direction in axisymmetric turbulent wakes, planar turbulent jets and grid-generated decaying turbulence (Seoud & Vassilicos 2007; Valente & Vassilicos 2012; Isaza *et al.* 2014; Hearst & Lavoie 2014; Nagata *et al.* 2013, 2017; Vassilicos 2015; Obligado *et al.* 2016; Chongsiripinyo & Sarkar 2020; Cafiero & Vassilicos 2019). These streamwise and temporal turbulence dissipation scalings reflect a non-equilibrium turbulence cascade characterised by a cascade time-lag between turbulent kinetic energy and integral length-scale on the one hand and turbulence dissipation on the other (Goto & Vassilicos 2015, 2016*a,b*). The cross-stream turbulence dissipation scaling (4.1) has its roots in the qualitatively different cross-stream spatial distribution of the incoherent turbulence kinetic energy on the one hand and the turbulence dissipation and/or integral length-scale on the other (see figure 18 where the quantities plotted are averaged over  $x$  but also recall that there is no such average in (4.1)). These different cross-stream spatial distributions are dislocations within the incoherent turbulence which are different from, but may nevertheless be somehow related to, the observed dislocation between the coherent energy  $\tilde{k}$  and the incoherent turbulence. More importantly, however, these dislocations within the incoherent turbulence may be somehow analogous to the cascade time-lag and may therefore be a reflection of a non-homogeneous turbulence cascade operating through space as well as time, very much like the cascade time-lag is an essential property of the non-equilibrium turbulence cascade. The scaling (4.1) implies that a new concept of a non-homogeneous turbulence cascade may be meaningful and complementary to the concept of non-equilibrium turbulence cascade, and may therefore be worth investigating in the future.



**Acknowledgements.** The experiments could be carried out thanks to the support of EL-SAT2020 project supported by the European Community, the French Ministry for Higher Education and Research, and the Hauts de France Regional Council in connexion with CNRS Research Foundation on Ground Transport and Mobility.

**Funding.** This work was supported by JCV's Chair of Excellence CoPreFlo funded by I-SITE-ULNE(grant number R-TALENT-19-001-VASSILICOS); MEL(grant number CONVENTION\_219\_ESR\_06) and Region Hauts de France (grant number 20003862).

**Declaration of interests.** The authors report no conflict of interest.

**Appendix: Proper Orthogonal Decomposition (POD)** In the present work, a POD method is used to separate the coherent motions in the flow from the remaining smaller scale motions. The POD method, which was first introduced in the study of turbulence by Lumley (1967), is now a well established technique for identifying the coherent motions (see Berkooz *et al.* 1993). In the present study we use the snapshot POD method (Sirovich 1987). The mathematical description of POD in a general Hilbert space is available in Holmes *et al.* (2012). Here we give a brief practical summary for the purpose of explaining what was done for this paper.

The velocity fluctuations  $u(x, y, t)$  and  $v(x, y, t)$  from the PIV measurement are arranged in a snapshot matrix  $\mathbf{U}$ , each column of which is composed of velocity fluctuations from the same PIV image:

$$\mathbf{U}_{(2m \times n)} = \begin{bmatrix} u_{x_1, y_1, t_1} & u_{x_1, y_1, t_2} & \cdots & u_{x_1, y_1, t_n} \\ u_{x_2, y_2, t_1} & u_{x_2, y_2, t_2} & \cdots & u_{x_2, y_2, t_n} \\ \vdots & \vdots & \ddots & \vdots \\ u_{x_m, y_m, t_1} & u_{x_m, y_m, t_2} & \cdots & u_{x_m, y_m, t_n} \\ v_{x_1, y_1, t_1} & v_{x_1, y_1, t_2} & \cdots & v_{x_1, y_1, t_n} \\ v_{x_2, y_2, t_1} & v_{x_2, y_2, t_2} & \cdots & v_{x_2, y_2, t_n} \\ \vdots & \vdots & \ddots & \vdots \\ v_{x_m, y_m, t_1} & v_{x_m, y_m, t_2} & \cdots & v_{x_m, y_m, t_n} \end{bmatrix} \quad (5.1)$$

where  $m$  is the number of data points in the image, e.g.  $m = 209 \times 249$  for SFV2.5, and  $n = 2000$  is the number of images in one run of the PIV measurement. (Note that for each SFV, measurements were taken over 10 runs.) The correlation matrix  $\mathbf{C}$  is the product of the transpose of  $\mathbf{U}$  with itself, i.e.

$$\mathbf{C}_{(n \times n)} = \mathbf{U}_{(n \times 2m)}^T \mathbf{U}_{(2m \times n)}. \quad (5.2)$$

Then we solve the eigenvalue problem

$$\mathbf{C}\boldsymbol{\phi}_i = \lambda_i \boldsymbol{\phi}_i \quad (5.3)$$

where  $\boldsymbol{\phi}_i$  ( $i = 1, 2, \dots, n$ ) is the eigenvector with  $n$  components and  $\lambda_i$  is the corresponding eigenvalue. The energy of each mode as a fraction of the total kinetic energy can be expressed as

$$E_i = \frac{\lambda_i}{\sum_{k=1}^n \lambda_k} \quad (5.4)$$

We can project the snapshot matrix  $\mathbf{U}$  onto each eigenvector and get the corresponding

spatial coefficients

$$[\mathbf{a}_1, \mathbf{a}_2, \dots, \mathbf{a}_n]_{(2m \times n)} = \mathbf{U}_{(2m \times n)} [\boldsymbol{\phi}_1, \boldsymbol{\phi}_2, \dots, \boldsymbol{\phi}_n]_{(n \times n)} \quad (5.5)$$

Because the correlation matrix  $\mathbf{C}$  is symmetric, the eigenvector matrix  $[\boldsymbol{\phi}_1, \boldsymbol{\phi}_2, \dots, \boldsymbol{\phi}_n]$  is orthogonal, i.e.  $[\boldsymbol{\phi}_1, \boldsymbol{\phi}_2, \dots, \boldsymbol{\phi}_n]^{-1} = [\boldsymbol{\phi}_1, \boldsymbol{\phi}_2, \dots, \boldsymbol{\phi}_n]^T$ . Therefore,

$$\begin{aligned} \mathbf{U}_{(2m \times n)} &= [\mathbf{a}_1, \mathbf{a}_2, \dots, \mathbf{a}_n] [\boldsymbol{\phi}_1, \boldsymbol{\phi}_2, \dots, \boldsymbol{\phi}_n]^T \\ &= \sum_{i=1}^n \mathbf{a}_i \boldsymbol{\phi}_i^T \\ &= \mathbf{U}_1 + \mathbf{U}_2 + \mathbf{U}_3 + \dots + \mathbf{U}_n \end{aligned} \quad (5.6)$$

which means physically  $\mathbf{U}$  can be decomposed into  $\mathbf{U}_i$  ( $\equiv \mathbf{a}_i \boldsymbol{\phi}_i^T$ ) contributed by different velocity modes. The relative kinetic energy contribution from different modes to the whole flow field is proportional to the value of the corresponding eigenvalue (5.4). Usually, the eigenvalues are sorted in descending order, therefore the first few modes  $\mathbf{U}_i$  which make the predominant contribution to the total turbulent kinetic energy can be treated as modes of the coherent motions.

#### REFERENCES

- ALAM, M. M. & ZHOU, Y. 2013 Intrinsic features of flow around two side-by-side square cylinders. *Phys. Fluids* **25** (8), 085106.
- ALAM, M. M., ZHOU, Y. & WANG, X. W. 2011 The wake of two side-by-side square cylinders. *J. Fluid Mech.* **669**, 432–471.
- ALVES PORTELA, F., PAPADAKIS, G. & VASSILICOS, J. C. 2018 Turbulence dissipation and the role of coherent structures in the near wake of a square prism. *Phys. Rev. Fluids* **3** (12), 124609.
- AVELAR, M. 2019 Spatial evolution of wakes generated by side by side cylinders. PhD thesis, Department of Aeronautics, Imperial College London.
- BATCHELOR, G. K. 1953 *The theory of homogeneous turbulence*. Cambridge university press.
- BEAULAC, S. & MYDLARSKI, L. 2004 Dependence on the initial conditions of scalar mixing in the turbulent wake of a circular cylinder. *Phys. Fluids* **16** (8), 3161–3172.
- BERKOOZ, G., HOLMES, P. & LUMLEY, J. L. 1993 The proper orthogonal decomposition in the analysis of turbulent flows. *Annu. Rev. Fluid Mech* **25** (1), 539–575.
- CAFIERO, G. & VASSILICOS, J.C. 2019 Non-equilibrium turbulence scalings and self-similarity in turbulent planar jets. *Proc. R. Soc. Lond. A* **475** (2225), 20190038.
- CAFIERO, G. & VASSILICOS, J. C. 2020 Non-equilibrium scaling of the turbulent-nonturbulent interface speed in planar jets. *Phys. Rev. Lett.* **125** (17), 174501.
- CARLIER, J. & STANISLAS, M. 2005 Experimental study of eddy structures in a turbulent boundary layer using particle image velocimetry. *J. Fluid Mech.* **535**, 143.
- CHEN, J. G., ZHOU, Y., ANTONIA, R. A. & ZHOU, T. M. 2018 Characteristics of the turbulent energy dissipation rate in a cylinder wake. *J. Fluid Mech.* **835**, 271–300.
- CHEN, J. G., ZHOU, Y., ANTONIA, R. A. & ZHOU, T. M. 2019 The turbulent Kármán vortex. *J. Fluid Mech.* **871**, 92–112.
- CHEN, J. G., ZHOU, Y., ANTONIA, R. A. & ZHOU, T. M. 2020 Temperature correlations with vorticity and velocity in a turbulent cylinder wake. *Int. J. Heat Fluid Flow* **84**, 108606.
- CHONGSIRIPINYO, K. & SARKAR, S. 2020 Decay of turbulent wakes behind a disk in homogeneous and stratified fluids. *J. Fluid Mech.* **885**, A31.
- DAIRAY, T., OBLIGADO, M. & VASSILICOS, J. C. 2015 Non-equilibrium scaling laws in axisymmetric turbulent wakes. *J. Fluid Mech.* **781**, 166–195.
- FOUCAUT, J.-M., CUVIER, C., COUDERT, S. & STANISLAS, M. 2016 3d spatial correlation tensor from an l-shaped spiv experiment in the vear wall region. In *Progress in wall turbulence 2* (ed. M. Stanislas, J. Jimenez & I. Marusic), pp. 405–417. Springer International Publishing.
- FOUCAUT, J.-M., GEORGE, W. K., STANISLAS, M. & CUVIER, C. 2020 Velocity derivatives in a high reynolds

- number turbulent boundary layer. part iii: Optimization of an spiv experiment for derivative moments assessment, arXiv: 2010.09364.
- FRISCH, U. 1995 *Turbulence: the legacy of A. N. Kolmogorov*. Cambridge university press.
- GEORGE, W. K. & HUSSEIN, H. J. 1991 Locally axisymmetric turbulence. *J. Fluid Mech.* **233**, 1–23.
- GOTO, S. & VASSILICOS, J. C. 2015 Energy dissipation and flux laws for unsteady turbulence. *Phys. Lett. A* **379** (16), 1144 – 1148.
- GOTO, S. & VASSILICOS, J. C. 2016a Local equilibrium hypothesis and Taylor’s dissipation law. *Fluid Dyn. Res.* **48** (2), 021402.
- GOTO, S. & VASSILICOS, J. C. 2016b Unsteady turbulence cascades. *Phys. Rev. E* **94** (5), 053108.
- HAYAKAWA, M. & HUSSAIN, F. 1989 Three-dimensionality of organized structures in a plane turbulent wake. *J. Fluid Mech.* **206**, 375–404.
- HEARST, R. J. & LAVOIE, P. 2014 Decay of turbulence generated by a square-fractal-element grid. *J. Fluid Mech.* **741**, 567–584.
- HOLMES, P., LUMLEY, J. L., BERKOOZ, G. & ROWLEY, C. W. 2012 *Turbulence, coherent structures, dynamical systems and symmetry*. Cambridge university press.
- ISAZA, J. C., SALAZAR, R. & WARHAFT, Z. 2014 On grid-generated turbulence in the near-and far field regions. *J. Fluid Mech.* **753**, 402.
- ISHIGAI, S. & NISHIKAWA, E. 1975 Experimental study of structure of gas flow in tube banks with tube axes normal to flow part ii; on the structure of gas flow in single-column, single-row, and double-rows tube banks. *Bulletin of JSME* **18** (119), 528–535.
- KIM, J. & DURBIN, P. A. 1988 Investigation of the flow between a pair of circular cylinders in the flopping regime. *J. Fluid Mech.* **196**, 431–448.
- KOLÁŘ, V., LYN, D. A. & RODI, W. 1997 Ensemble-averaged measurements in the turbulent near wake of two side-by-side square cylinders. *J. Fluid Mech.* **346**, 201–237.
- KOLMOGOROV, A. N. 1941a Dissipation of energy in locally isotropic turbulence. *Dokl. Akad. Nauk SSSR* **32**, 16–18.
- KOLMOGOROV, A. N. 1941b The local structure of turbulence in incompressible viscous fluid for very large Reynolds numbers. *Dokl. Akad. Nauk SSSR* **30**, 301–305.
- KOLMOGOROV, A. N. 1941c On degeneration (decay) of isotropic turbulence in an incompressible viscous liquid. In *Dokl. Akad. Nauk SSSR*, , vol. 31, pp. 538–540.
- LAVOIE, P., AVALLONE, G., DE GREGORIO, F., ROMANO, G. P. & ANTONIA, R. A. 2007 Spatial resolution of pIV for the measurement of turbulence. *Exp. Fluids* **43** (1), 39–51.
- LECORDIER, BERTRAND & TRINITE, MICHEL 2004 Advanced pIV algorithms with image distortion validation and comparison using synthetic images of turbulent flow. In *Particle image velocimetry: recent improvements*, pp. 115–132. Springer.
- LEFEUVRE, N., THIESSET, F., DJENIDI, L. & ANTONIA, R. A. 2014 Statistics of the turbulent kinetic energy dissipation rate and its surrogates in a square cylinder wake flow. *Phys. Fluids* **26** (9), 095104.
- LUMLEY, J. L. 1967 The structure of inhomogeneous turbulence. In *Atmospheric Turbulence and Radio Wave Propagation* (ed. A. M. Yaglom & V. I. Tatarski), pp. 166–178. Moscow.
- NAGATA, K., SAIKI, T., SAKAI, Y., ITO, Y. & IWANO, K. 2017 Effects of grid geometry on non-equilibrium dissipation in grid turbulence. *Phys. Fluids* **29** (1), 015102.
- NAGATA, K., SAKAI, Y., INABA, T., SUZUKI, H., TERASHIMA, O. & SUZUKI, H. 2013 Turbulence structure and turbulence kinetic energy transport in multiscale/fractal-generated turbulence. *Phys. Fluids* **25** (6), 065102.
- NEDIĆ, J., TAVOULARIS, S. & MARUSIC, I. 2017 Dissipation scaling in constant-pressure turbulent boundary layers. *Phys. Rev. Fluids* **2** (3), 032601.
- NEDIĆ, J., VASSILICOS, J. C. & GANAPATHISUBRAMANI, B. 2013 Axisymmetric turbulent wakes with new nonequilibrium similarity scalings. *Phys. Rev. Lett.* **111** (14), 144503.
- OBLIGADO, M., DAIRAY, T. & VASSILICOS, J. C. 2016 Nonequilibrium scalings of turbulent wakes. *Phys. Rev. Fluids* **1** (4), 044409.
- ORTIZ-TARIN, J. L., NIDHAN, S. & SARKAR, S. 2021 High-Reynolds-number wake of a slender body. *J. Fluid Mech.* **918**.
- POPE, S. B. 2000 *Turbulent Flows*. Cambridge University Press.
- RUBINSTEIN, R. & CLARK, T. T. 2017 “equilibrium” and “non-equilibrium” turbulence. *Theor. App. Mech. Lett.* **7** (5), 301–305.
- SCARANO, FULVIO 2001 Iterative image deformation methods in pIV. *Measurement science and technology* **13** (1), R1.

- SELOUD, R. E. & VASSILICOS, J. C. 2007 Dissipation and decay of fractal-generated turbulence. *Phys. Fluids* **19** (10), 105108.
- SIROVICH, L. 1987 Turbulence and the dynamics of coherent structures. i. coherent structures. *Quart. Appl. Math.* **45** (3), 561–571.
- SORIA, JULIO 1996 An investigation of the near wake of a circular cylinder using a video-based digital cross-correlation particle image velocimetry technique. *Experimental Thermal and Fluid Science* **12** (2), 221–233.
- SUMNER, D., WONG, S. S. T., PRICE, S. J. & PAIDOUSSIS, M. P. 1999 Fluid behaviour of side-by-side circular cylinders in steady cross-flow. *J. Fluids Struct.* **13** (3), 309–338.
- TAYLOR, G. I. 1935 Statistical theory of turbulence iv-diffusion in a turbulent air stream. *Proc. R. Soc. Lond. A* **151** (873), 465–478.
- TAYLOR, G. I. 1938 The spectrum of turbulence. *Proc. R. Soc. Lond. A* **164** (919), 476–490.
- TENNEKES, H. & LUMLEY, J. L. 1972 *A first course in turbulence*. MIT press.
- TOKGOZ, S., ELSINGA, G. E., DELFOS, R. & WESTERWEEL, J. 2012 Spatial resolution and dissipation rate estimation in taylor–couette flow for tomographic piv. *Exp. Fluids* **53** (3), 561–583.
- VALENTE, P. C. & VASSILICOS, J. C. 2012 Universal dissipation scaling for nonequilibrium turbulence. *Phys. Rev. Lett.* **108** (21), 214503.
- VASSILICOS, J. C. 2015 Dissipation in turbulent flows. *Annu. Rev. Fluid Mech.* **47**, 95–114.
- WILLERT, CHRISTIAN E & GHARIB, MORTEZA 1991 Digital particle image velocimetry. *Experiments in fluids* **10** (4), 181–193.
- XU, S. J., ZHOU, Y. & SO, R. M. C. 2003 Reynolds number effects on the flow structure behind two side-by-side cylinders. *Phys. Fluids* **15** (5), 1214–1219.
- YASUDA, T. & VASSILICOS, J. C. 2018 Spatio-temporal intermittency of the turbulent energy cascade. *J. Fluid Mech.* **853**, 235–252.
- YEN, S. C. & LIU, J. H. 2011 Wake flow behind two side-by-side square cylinders. *Int. J. Heat Fluid Flow* **32** (1), 41 – 51.
- ZHOU, Y. & ANTONIA, R. A. 1993 A study of turbulent vortices in the near wake of a cylinder. *J. Fluid Mech.* **253**, 643.
- ZHOU, Y., NAGATA, K., SAKAI, Y. & WATANABE, T. 2019 Extreme events and non-kolmogorov  $-5/3$  spectra in turbulent flows behind two side-by-side square cylinders. *J. of Fluid Mech.* **874**, 677–698.
- ZHOU, Y. & VASSILICOS, J. C. 2017 Related self-similar statistics of the turbulent/non-turbulent interface and the turbulence dissipation. *J. Fluid Mech.* **821**, 440–457.
- ZHOU, Y., ZHANG, H. J. & YIU, M. W. 2002 The turbulent wake of two side-by-side circular cylinders. *J. Fluid Mech.* .